

Functional Degradation and Self-enhanced Elastocaloric Cooling Performance of NiTi Tubes under Cyclic Compression

Dingshan Liang^{1,2}, Peng Hua¹, Junyu Chen³, Fuzeng Ren^{2,*}, Qingping Sun^{1,*}

¹Department of Mechanical and Aerospace Engineering, The Hong Kong University of Science and Technology, Clear Water Bay, Kowloon, Hong Kong, China

²Department of Materials Science and Engineering, Southern University of Science and Technology, Shenzhen, Guangdong, China

³Department of Engineering Mechanics, School of Civil Engineering, Wuhan University, Wuhan, Hubei, China

Corresponding Author. E-mail: renfz@sustech.edu.cn; meqpsun@ust.hk

Abstract

Superelastic NiTi tubes are promising candidates for eco-friendly elastocaloric cooling, but their cyclic stability suffers severely from functional degradation. Herein, we investigate the functional degradation of nanocrystalline NiTi tubes via in-depth analysis and find out that it is beneficial to elastocaloric cooling performance. The results show that the functional degradation accompanies with progressive accumulation of residual strain and significant reduction in both hysteresis loop area

(D) and forward transformation stress (σ_f^{tr}). The accumulation of residual strain arises from phase-transition-induced dislocations and dislocation-pinned residual martensite. The former separates the original austenite grains to much smaller nanodomains (equivalent to grain size effect) and contributes to the strain hardening during phase transition, leading to the significant reduction of D . The latter induces compressive residual stress in the austenite phase and thus gives rise to the evolutive reduction of σ_f^{tr} . Consequently, the material coefficient of performance (COP_{mater}) was self-enhanced for 40~104 %. The beneficial effect is mainly because of the cyclically-decreased D . The study might provide a processing route to tailor COP_{mater} and stabilize the mechanical response of NiTi by cyclic compression.

Keywords: Elastocaloric cooling; Cyclic response; NiTi; Shape memory alloy (SMA); Martensitic phase transformation.

1. Introduction

In recent years, solid-state cooling using green elastocaloric materials has emerged as an active field of research [1-3]. Superelastic NiTi shape memory alloy (SMA) has been employed as a promising core element in the bulk refrigeration prototypes, due to its large latent heat under stress-induced phase transition (PT) [4-7]. An external applied stress is required to convert the solid-state austenite phase (B2) to solid-state martensite phase (B19') and the latent heat is released to the surroundings, leading to a temperature increase. With the stress being removed, B19' transforms to B2 reversely and the same amount of latent heat is absorbed from the surroundings, leading to a temperature drop [8, 9]. Such reversible PT of NiTi can be utilized in solid-state refrigerators based on the elastocaloric effect [10-15]. Of all the stress-loading modes, cyclic compression of bulk superelastic NiTi tubes is favored for elastocaloric cooling, because the tube configuration has the following advantages: (1) much improved fatigue resistance via suppression of crack initiation and growth (up to 78 million), (2) macroscopically homogeneous stress and strain, and (3) efficient heat transfer from the material to the heat transfer fluid [16-20].

However, conventional bulk NiTi SMA suffers from severe functional degradation, which is manifested as the fast accumulation of residual strain (ϵ^{res}) and decreases in the hysteresis loop area (D) and the forward transformation stress (σ_f^{tr}) in the first several hundreds of cycles [18, 21-25]. The macroscopic functional degradation in superelasticity strongly affects the functional performance of NiTi SMA in damping structure [26] and actuators [27]. It is well known that such functional degradation

originates from the lattice mismatch between B2 and B19'[28, 29]. Under external loading, the mismatch at the atomic scale results in high stress concentration at the habit planes (interface of B2 and B19') during PT and thus leads to the formation of dislocations [30-32]. Subjected to cyclic loading, the habit planes swipe through the grain interior and even across grain boundaries. Owing to the PT-induced dislocations block the movement of habit planes and suppress the reverse transition of martensite, irreversible residual martensite is constrained at the microscale and the resultant residual stresses are induced in both austenite and martensite phases [23, 33-35]. Such microstructural changes of NiTi under cyclic PT are responsible for the macroscopic functional degradation, which can be reflected from the evolution of the isothermal stress-strain ($\sigma\sim\varepsilon$) responses. Concerning the well-studied mechanisms of functional degradation were mainly characterized under cyclic tension, the fundamental mechanisms under cyclic compression of bulk NiTi require further investigation. Therefore, it is crucial to probe the functional degradation of NiTi tube under cyclic compression, which has not been well-explored, to correlate the microstructural evolution to the macroscopic responses.

Besides, the effects of functional degradation on the elastocaloric cooling performance of NiTi SMA has not been systematically studied. The reduction in the forward transformation stress can increase the transformation strain and temperature drop of NiTi under partial PT [5, 16]. And the decrease in the hysteresis loop area can decrease the amount of input work (w) for elastocaloric cooling [3, 36]. Therefore, the functional degradation of SMAs might be beneficial to the elastocaloric cooling

performance. It is essential to unravel the relation between functional degradation and elastocaloric cooling, so as to find the optimal working condition of NiTi.

In this work, cyclic compression of NiTi tubes under stress from partial to full PT were performed to evaluate the functional degradation and its effect on the elastocaloric cooling performance. Residual stress and volume fraction of B2 and B19' were measured from X-ray diffraction (XRD). Microstructural evolution was examined by transmission electron microscopy (TEM). Subsequently, the roles of PT-induced dislocations and residual martensite on the evolution of mechanical responses were analyzed. Finally, the effects of functional degradation on the elastocaloric cooling performance were evaluated. The study provides possible routes to optimize the functional performance of NiTi tubes via cyclic compression.

2. Materials and methods

2.1 Materials and characterization

Bulk NiTi tubes (Vascotube, Germany) had a wall thickness of 0.55 mm with an outer diameter of 5 mm and contained 50.57 at.% Ti as determined by energy dispersive X-ray spectroscopy (EDX, Oxford Instruments, UK). The austenite finish temperature (A_f) was determined to be 21.6 °C by differential scanning calorimeter (DSC; TA Q1000, USA) ranging from – 80 °C to 100 °C at a rate of 10 °C/min (Fig. S1). The phase composition was identified using X-ray diffraction (XRD, Rigaku Smartlab-9 kW, Japan) in a 2θ range from 35° to 50° at a step size of 0.01° and a scan rate of 10° min⁻¹. The *in situ* XRD was conducted at a heating/cooling rate of 10 °C/min and held for 20

minutes at each tested temperature. The quantitative analysis were evaluated via Rietveld refinement in MAUD. The microstructure was examined by TEM (200 kV, JEOL 2010, Japan and 300 kV, FEI Tecnai G2 F30, USA). The TEM thin foils were lifted out from the middle section of the tubes using focus ion beam system (FIB; FEI Helios G4, USA).

2.2 Mechanical testing set up

The mechanical tests were performed on an MTS machine (Landmark 370.10, USA) with a specially designed compression fixture for NiTi tubes (Fig. S2a). The temperature of clamped tubes under MTS frame is ~ 30 °C, which is above A_f . The *in-situ* temperature profile was captured by an infrared camera (FLIR SC7700M, USA). The NiTi tubes were cut into 22.5 mm (with an effective height of 12.5 mm; Fig. S2b) in height by electrical discharge machining. The radial direction, axial direction and tangential direction were denoted as RD, AD and TD. Theoretical estimation showed that the tubes would not buckle under the present testing conditions (details can be found in Part 3 of Supplementary data). And it has also been confirmed by the experimental observations during cyclic compression.

To determine the strain of the tubes, empty tests were run first without tubes to determine the force-displacement relation of the compression fixture and the MTS frame. All the data obtained from the MTS system were proceeded to eliminate the displacement of the compression fixture and the MTS frame for a relatively accurate displacement of tested tubes.

2.3 Cyclic compression, isothermal test, and COP measurement

The compressive stress-strain curve (Fig. S3) of the as-received NiTi tubes show that σ_f^{tr} is approximately 617 MPa at room temperature. Thus, three maximum applied loads (σ_{max}) of 800, 1000 and 1200 MPa were selected to study the cyclic response from partial PT to full PT. Cyclic compression were conducted at a frequency of 4 Hz to accumulate cycle number (N). It was stopped after certain cycles to perform isothermal compression at a loading rate of 6 N/s and *COP* measurement. The *COP* measurements were conducted for five cycles right after the isothermal compression. The procedure is set as: 1) adiabatic loading to σ_{max} in 0.2 s; 2) holding the displacement for 70 s to transfer heat to air ambient; 3) adiabatic unloading to 50 MPa in 0.2 s; 4) holding the displacement for 70 s to transfer heat to air ambient. The obtained last four cycles in the *COP* measurement, including the complete circle of the thermodynamic cycle, were used to analyze the mechanical input work, adiabatic temperature drop (ΔT_c) and COP_{mater} .

2.4 Temperature dependence of the forward transformation stress

Three tubes were loaded to 1200 MPa at a loading rate of 6 N/s on an Instron 5969 testing machine (USA) with a furnace at 25 , 35 and 45 °C. The forward transformation stress and phase transformation strain (ϵ^{tr}) were obtained from the isothermal strain-stress curve.

2.5 Removal of residual martensite via low-temperature heating

A tube was cyclically compressed under σ_{max} of 1200 MPa at 4 Hz for 10^4 cycles and the change of height was recorded to study the quantitative contribution of residual strain. The deformed tube was heated at 100 °C for 20 minutes and XRD was performed on the surface after it was cooled to room temperature. Then, two cycles of isothermal compression were conducted to make a comparison with the non-heated tube. Finally, the heated tube was stabilized to $\varepsilon^{res} = 3.88$ % with another 10^4 cycles. The *in situ* XRD was carried on the tube surface after 2×10^4 cycles with a residual strain of 3.88%. The XRD on the RD-TD plane were performed on the as-received, deformed ($\varepsilon^{res} = 3.88$ %) and heated specimens.

3. Results and discussions

3.1 Basic features of NiTi tubes

The as-received tubes have nano-laminated gains with an average layer thickness of 78 nm (Fig. 1a). The selected area diffraction pattern (SADP) confirms the presence of B2 austenite at room temperature and the texture is mainly $\langle 110 \rangle // RD$ (inset of Fig. 1a). The typical grain size of B2 (110) is about 44 nm (bright in Fig. 1b). At 25 °C, σ_f^{tr} is 613 MPa and ε^{tr} is 3.1 % (Fig. 1c). ε^{res} is 0.4 %, 0.51 % and 1.04 % at 25 °C, 35 °C and 45 °C under 1200 MPa, indicating higher temperature coupling with higher σ_f^{tr} results in a higher degree of irreversibility during the reverse PT. As reported in the literatures [4, 6, 37, 38], the temperature dependence of σ_f^{tr} is linear as fitted in Fig. 1d. The Clausius-Clapeyron slope (K_f) is determined to be 12.04 MPa/°C. Based on the Clausius-Clapeyron equation, the transition entropy change (ΔS) can be evaluated from

$\Delta S = -K_f \cdot \varepsilon^{tr}$ [15]. At 25 °C, $\Delta S = -0.37324$ MJ/(m³·°C). Take the density of NiTi as 6500 kg/m³, ΔS is as large as -57.4 J/(kg·°C). Of particular note is that the tube can produce an adiabatic temperature drop of 25 °C during reverse PT under a preloading stress of 800 MPa (see Part 5 in Supplementary data). In short, the NiTi tubes have a large transition entropy change and demonstrate promising cooling potential.

3.2 Functional degradation of NiTi tubes

3.2.1 Evolution of the isothermal $\sigma\sim\varepsilon$ responses

The functional degradation of NiTi tubes can be reflected from the evolution of compressive $\sigma\sim\varepsilon$ responses under 800, 1000 and 1200 MPa. As shown in Fig. 2, the functional degradation displays as the accumulation of ε^{res} and the reduction in σ_f^{tr} and D . The isothermal $\sigma\sim\varepsilon$ curves evolve from the typical plateau type at the beginning to a strain-hardening one as the cycle accumulates. Based on the slope transition, the phase transformation stresses can be determined and the loading stage of the $\sigma\sim\varepsilon$ curves can be divided as the elastic deformation of B2 (E_{B2}), PT (B2→B19') and elastic deformation of B19' ($E_{B19'}$). The reverse transformation stress (σ_r^{tr}) with nonobvious slope transition was determined as the stress at the same strain of σ_f^{tr} during unloading.

Under σ_{max} of 800 MPa (Fig. 2a), the NiTi tube undergoes partial PT with a ε^{tr} of 2.5%, and there appears to be no sign of $E_{B19'}$ from the $\sigma\sim\varepsilon$ curve at $N = 1$. The $\sigma\sim\varepsilon$ curve changes from a broad PT hysteresis loop to a narrow one when the cycle increases. Meanwhile, E_{B2} couples with PT and more amount of B2 can be transformed to B19'

since σ_f^{tr} keeps decreasing. Such evolution can be confirmed by the cyclically-increased temperature change under 4 Hz after 100 cycles (Noted in Fig. 2a, see Part 6 in Supplementary data for detail). The quicker the temperature rises versus time after certain cycles of compression (Fig. S5b-c), which is consistent with the reduction of σ_f^{tr} .

For tubes under 1000 MPa (Fig. 2b) and 1200 MPa (Fig. 2c), full PT can be achieved since $E_{B19'}$ can be determined from the increase of slope after the PT plateau in the first cycle. Akin to the case under 800 MPa, σ_f^{tr} and D decrease dramatically as the cycle increases. Under 1000 MPa, the $\sigma\sim\varepsilon$ curve changes from a large open loop to an enclosed middle-narrow one with sharp ends. As for 1200 MPa, it develops from a huge middle-wide loop to a curved “needle” tilted to the top-right. Such geometrical changes in the hysteresis, accounting for the strain hardening at the stage of $E_{B19'}$, might be attributed to the martensite reorientation [39-41].

The detailed evolutions of ε^{res} , $\frac{d\varepsilon^{res}}{dN}$, σ_f^{tr} , σ_r^{tr} , D and $\frac{dD}{dN}$ were plotted versus cycle N in Fig. 3 to study the functional degradation. These evolutions demonstrate linear relationships in the logarithmic scale before saturation. That is, the macroscopic degradation features obey the power-law relationships similar to that at the microscale [29], while the cyclic effect is much faster. The height change of the tubes reveals the residual strain due to cyclic compression (Fig. 3a). Gradually, the residual strains stabilize at 1.34 %, 2.86 % and 3.88 % under σ_{max} of 800, 1000 and 1200 MPa after 10^3 cycles. The accumulation rate of ε^{res} demonstrates a monotonical manner to decrease with increasing N and becomes 4 orders lower after 4×10^3 cycles under σ_{max} of 800 MPa,

as small as 10^{-7} per cycle. It drops to 0 after 10^3 ($\sigma_{max} = 1000$ MPa) and 4×10^3 ($\sigma_{max} = 1000$ MPa) cycles, without appearing in the logarithm scale in Fig. 3b. Overall, The residual strain is highly sensitive to σ_{max} and higher σ_{max} leads to quicker stabilization to a larger saturated magnitude after 10^3 cycles.

Similarly, σ_f^{tr} drops significantly in the first 400 cycles and gradually stabilizes after 10^3 cycles (Fig. 3c). It can be reduced to as low as 177 MPa ($\sigma_{max} = 1000$ MPa) and 163 MPa ($\sigma_{max} = 1200$ MPa) at $N=10^4$, which is only one third of that at $N = 1$. Likewise, σ_r^{tr} behaves in a tendency to reduce as N increases (Fig. 3d). Both σ_f^{tr} and σ_r^{tr} are in a higher level with respect to lower σ_{max} . The hysteresis loop area, which reflects the hysteresis heat [42], keeps decreasing in power-law relation and reaches to an analogous magnitude below 2 MPa at $N=10^4$. The reduced D is about 5, 6.5, and 8 times smaller than that at $N = 1$ for σ_{max} of 800, 1000 and 1200 MPa (Fig. 3e). The decreasing rate of D (dD/dN) drops significantly to the scale of 10^{-4} MPa/cycle after 4×10^3 cycles, which is about 5 orders lower than that at the beginning (Fig. 3f). Overall, higher σ_{max} results in quicker stabilization within 10^3 cycles and larger amount of degradation.

3.2.2 *Cyclically-induced residual martensite*

To seek the origins of the functional degradation, we performed XRD characterization on the middle section of tubes after 10^4 cycles and made comparisons with the as-received tube. The diffraction profiles were taken under the same conditions and indexed by B2 (JCPDS No. 65-0917) and B19'(JCPDS No. 65-0145). Such

comparisons can provide solid evidence of the phase evolution due to cyclic compression.

Compared with the as-received tube, the diffraction peak of B2 (110) of the cyclically-deformed tubes at $N = 10^4$ show three distinct features with the increase of σ_{max} : (i) shift to a larger 2θ ; (ii) pronounced peak broadening; and (iii) much weaker intensity (Fig. 4a). These observations suggest the formation of lattice strain, buildup of dislocations and size reduction of B2. In contrast, the characteristic peaks of B19' become significantly stronger in the cyclically-deformed tubes (Fig. 4b). Evidenced by the presence of B19' (012), the residual martensite coexisted with austenite in the cyclically-deformed tubes and higher σ_{max} refers to a greater amount of residual martensite.

Based on the shift in the d -spacing (Bragg's law: $2d\sin\theta = n\lambda$), the uniform lattice strain can be calculated via the following equation [23].

$$\varepsilon_{hkl} = \frac{d_{hkl}^{deformed} - d_{hkl}^{as-received}}{d_{hkl}^{as-received}} \quad (1)$$

The lattice strain from the indexed planes is plotted in Fig. 4c. It is found that the lattice strain of B2 (110) and B19' (002) are in an equivalent magnitude but the sign is opposite. It is compressive for B2 (110) while tensile for B19' (002) along RD, demonstrating a higher degree of lattice strain under higher σ_{max} . Such distributions of internal strain filed reveal that the residual martensite is capable to coexist with austenite without external stress, similar to the observed results under cyclic tension [23, 43, 44]. Concerning to the compressive lattice strain on B2 (110), the residual stress is estimated based on the elastic modulus of B2 (110) ($E_{110}^{B2} = 74.7$ GPa) under compression [41].

The residual stress of B2 (110) at $N = 10^4$ is higher with respect to higher σ_{max} (Fig. 4d). Although this residual stress is along RD (perpendicular to the compression direction), such buildup of residual stress in B2 may be responsible for the progressive change in σ_f^{tr} .

The full width at half maximum (FWHM) of B2 (110) tends to increase with respect to higher σ_{max} , suggesting a higher degree of grain size reduction and/or lattice distortion in B2 under higher σ_{max} (Fig. 4e). To further understand the effect of residual martensite on the functional degradation, we estimate the volume fraction of B2 and B19' via Rietveld refinement (Fig. 4f). Detailed refinement analysis can be found in Fig. S6. The results show that the as-received tube contains 2.4 % of martensite, which might be induced by the processing of tube-drawing and the near room temperature A_f . The volume fraction of residual martensite increases to be 18.4%, 31.6% and 37.7% for the cyclically-deformed tubes under σ_{max} of 800, 1000 and 1200 MPa. It shows that higher σ_{max} leads to a greater amount of residual martensite. Considering similar tendency of residual strain, the residual martensite may contribute to the residual strain at the macroscopic scale.

3.2.3 *Cyclically-deformed microstructure: the role of dislocations*

For further observation at microscale, we examined the microstructure of the tube after 10^4 cycles of compression under $\sigma_{max} = 1200$ MPa, which has the highest level of macroscopic residual strain. As shown in Fig. 5a, the microstructure of cyclically-deformed tube is significantly different from the original nano-laminated structure, and

residual martensite (B19') is found from the SAED pattern (inset of Fig. 5a). It is notable that the original texture shows very intense diffraction spots of B2 (110) in parallel to RD (Fig. 1a). However, the texture of deformed tube demonstrates a main manner of B2 (110) in parallel to AD, which is the loading direction. The texture of B2 phase after 10^4 cycles of PT might be self-accommodated to the preferred orientation [45, 46].

The microstructural changes of B2 are mainly size reduction and dislocation slip. After 10^4 cycles of compression, the nano domains of B2 (110) are partitioned to ~ 9.5 nm by dislocation walls and distributed inside a one-hundred-nanometer B2 realm (Fig. 5b). Such size reduction, equivalent to grain size refinement, is in good agreement with the broadening in FWHM of B2 (110) (Fig. 4e). Note that smaller grain size has been proved to result in smaller hysteresis loop area of NiTi [36, 47, 48]. The significantly reduced size of B2 (110) in the cyclically-deformed tube may be responsible for the greatly decreased hysteresis loop area. Fig. 5c-d show the high-resolution TEM image and the selected area inverse fast Fourier transformation (IFFT) image of B2 austenite. Substantial intragranular lattice distortion is observed of B2 (Fig. 5c). Dislocation slips with Burgers vector of $\mathbf{b} = 0.298 \bar{1}10$ are found in a B2 grain (Fig. 5d). These imply that the compressive PT induce dislocation slip and lattice distortion in B2 austenite phase.

Severe lattice distortion of the residual martensite is observed in the high resolution TEM image (Fig. 5e). The lattice scale mismatch is found next to the residual martensite grain with a size of 20 nm. From the IFFT image (Fig. 5f) of the selected area in Fig.

5e, a high density of dislocation blocks and surrounds the grain of B19'. The dislocation density in the selected area is as high as $3.18 \times 10^{12} \text{ cm}^{-2}$, almost a half of that at the interface between crystalline and amorphous phase in cold-rolled NiTi [49]. The dislocation slip in B2 and dislocation-pinned martensite may be the main causes to the macroscopic residual strain, similar to the cyclic compression of NiTi micro pillar [29]. In addition, the surface roughness of the cyclically-deformed tubes slightly increases, which may be a result of PT-induced plastic deformation on the surface (Fig. S8).

Such lattice distortion inside a residual martensite grain reveals that the internal strain field plays an important role in the cyclically-deformed NiTi [50]. Regarding a high dislocation density and severe lattice dilation, the shear modulus would be softened according to the Grüneisen relation [49, 51]. That is, the PT (B2→B19') induced by shear deformation can be triggered easily. It is notable that the B2 grains are partitioned to tens of nanometers by dislocation walls under such high degree of lattice distortion. The size reduction of B2 indicates that the reversible PT could have occurred at lower energy barrier due to the continuous PT with habit planes moving forth and back within reduced domains pinned by dislocations, instead of the habit planes migrating through large grain and even grain boundaries [47]. Also, the dislocation-pinned residual martensite can serve as the nucleation origin of PT, without overcoming high energy barriers for B2 to initially transform to B19'. And thus the transformation stress is reduced during functional degradation. The gradual stabilization of NiTi tubes evolves from the discontinuous first-order PT at the beginning to continuous PT under high internal stress field coupled with dislocation-

blocked martensite. Such continuous PT in can permit SMA with small dissipation energy, leading to a small hysteresis loop area [36, 52, 53]. The isothermal $\sigma\sim\varepsilon$ curves also reflect the evolutionary transformation mode from first-order PT (segregation of E_{B2} and PT) to continuous PT (coupling of E_{B2} and PT) (Fig. 2). Consequently, the monotonically reduced hysteresis loop area could be sourced from the reduced size of dislocation-wall-separated B2 grain and the resultant continuous PT.

3.2.4 Removal of residual martensite via heating

Note that the residual martensite can be healed by heating [29, 54]. We further explore the mechanical responses, phase composition and microstructure after removal of residual martensite. Consequently, the effect of residual martensite on the macroscopic ε^{res} , σ_f^{tr} and D are analyzed.

We first analyze the variation of mechanical response and corresponding XRD due to heating. As plotted in Fig. 6a, the isothermal $\sigma\sim\varepsilon$ responses after heating (red solid line) represents a variation from stabilized small hysteresis loop (low σ_f^{tr} , $N = 10^4$) to enlarged open loop (increased σ_f^{tr} and partially-recovered ε^{res}). It is notable that the residual strain before heating is 3.8%, and it is in an equivalent magnitude to the tube without heating ($\varepsilon^{res} = 3.88\%$). The main effects of heating are partial recovered ε^{res} , enlarged D and increased σ_f^{tr} . Evidenced by the XRD pattern after heating, the intensity of the diffraction peaks of residual martensite reduced significantly, suggesting most of the residual martensite is thermally healed back to austenite (Fig. 6b). The characteristic peak of B2 (110) shifts to a smaller 2θ angle compared to the

deformed tube and still maintains a slight shift to the right with 0.15° , indicating that the high compressive residual stress in B2 evolves to a lower scale. This result confirms that the change of σ_f^{tr} is tightly linked to the compressive residual stress in the B2 phase.

In order to uncover the nature of stabilized microstructure, *in situ* XRD were performed on the deformed tube ($\epsilon^{res} = 3.88\%$, $N = 2 \times 10^4$) (Fig. 6c). Another 10^4 cycles were conducted after two cycles of isothermal compression and the residual strain is stabilized to 3.88 % (equivalent to the non-heating tube at $N = 10^4$). It indicates that the residual martensite can be removed by heating and recreated by cyclic loading, with the obvious change in residual strain. As the temperature cools from 25°C to -50°C , two key features are observed: 1) the intensity of B2 (110) decreases obviously while B19' (002) increases, especially at -50°C (blue line in Fig. 6c); 2) the position of B2 (110) shifts to the right while B19' (002) to the left. The former suggests that partial B2 is thermally transformed to B19' and B2 can coexist with B19' even at -50°C , which is well below the original A_f . This finding might be able to provide reversible PT of cyclically-deformed NiTi for the elastocaloric cooling at extremely low temperature. The latter reveals that higher degree of internal stress field, as well as lattice distortion reflected from the broadening and asymmetry of the shape of B2 (110), were formed at -50°C . Interestingly, such thermally-induced changes are reversible since the diffraction pattern can be recovered when it heated back to 25°C , demonstrating a two-way shape memory effect. Then the tube was heated to 100°C and held for 20 minutes, and the qualitative results consist with the comparison of XRD in Fig. 6b.

We then further correlate the residual stress along loading direction to the reduction of σ_f^{tr} , and hence XRD on the surface of the RD-TD plane were performed. Based on the peak shift, the residual stress of B2 (110) and (211) is compressive in the cyclically-deformed tube (Fig. 7a-b). After heating, such compressive residual stresses change to tensile residual stress and lower degree of compressive residual stress. As σ_f^{tr} of the deformed tube is decreased and it partially increases after heating, the compressive residual stress of B2 phase should be responsible for the reduction of σ_f^{tr} during functional degradation.

As a complement, we heated the TEM foil (lifted from the cyclically-deformed tube) at 100 °C for 20 minutes and observed the microstructure. The heated microstructure is similar to the cyclically-deformed one but no diffraction spot of B19' is observed from the SADP (Fig. 8a). It is basically B2 phase after the heating. Evaluating the average d -spacings of B2 (110) from the SADP (Fig. S8), the lattice strain after heating along AD is -0.006 , which is significantly lower than that before heating (-0.043). Although it is highly localized under TEM, it is consistent with the results of XRD along the loading direction. Regarding the significant reduction of σ_f^{tr} , it implies that the compression-parallel compressive residual stress accounts mostly for the reduction of σ_f^{tr} . To conclude, the significant reduction of σ_f^{tr} may source from the pile-up of compressive residual stress in the B2 phase.

After confirming the compressive residual stress in B2 lead to the reduction of σ_f^{tr} , we then further discuss the underlying mechanisms for the shrinkage of D . The amount of B2 (110) increases due to the heating (intensity in Fig. 7a). The dark field TEM image

further confirms that the grains of B2 (110) with size at tens of nanometers are hierarchically distributed inside the hundred-nanometer domains (Fig. 8b). These results are in good agreements to the comparisons of XRD (Fig. 6-7). Regarding that the hysteresis loop area enlarged while strain hardening remained after heating, the reduction of B2 domain size might be responsible for the strain hardening of the hysteresis loop, partly leading to the shrinkage of the hysteresis loop area. In the other hand, the larger reduction of σ_f^{tr} than that of σ_r^{tr} , which is induced by the internal stress field, results in the decrease of the difference between σ_f^{tr} and $\sigma_r^{tr}(\Delta\sigma^{tr})$. The linear relation between hysteresis loop area and $\Delta\sigma^{tr}$ discloses that the smaller $\Delta\sigma^{tr}$ couples with smaller hysteresis loop area (Fig. S9). Therefore, the shrinkage of hysteresis loop area is originated from the reduction of B2 domain size (strain hardening and lower dissipated energy) and internal stress field (reduction of σ_f^{tr}).

Finally, we estimate the effect of residual martensite on the macroscopic residual strain. After heating, about 1.2% of residual strain is recovered due to the thermal-induced restoration of residual martensite. Referring to the Rietveld refinement, the volume fraction of residual martensite is determined to be 0.6 % after heating. That is, about 37.1 % of residual martensite are thermally-transformed to austenite, recovering 1.2 % of residual strain. Since the transformation strain of the tube is 3.1% at room temperature, the residual strain contributed by residual martensite can be evaluated as : $\varepsilon_{B19'}^{res} = \varepsilon^{tr} \times V_{B19'}$, where $V_{B19'}$ is the volume fraction of contributed martensite. Therefore, $\varepsilon_{B19'}^{res}$ can be evaluated to be 1.15 % and it is well consistent with the recovered residual strain of 1.2%. The calculated result suggests that about 33% of the

residual strain is contributed from the residual martensite. The study on the cyclic behavior of NiTi micropillar also confirms that the residual martensite makes certain contribution to the residual strain [29].

3.2.5 Mechanisms of functional degradation

The functional degradation in the mechanical response of NiTi tubes is briefly described in Fig. 9a, demonstrating an overall tendency of accumulation of the residual strain, decrease in the forward transformation stress and shrinkage of the hysteresis loop area. As well explained under tension [23], the fundamental origins are the lattice mismatch in the interface between B2 and B19' and resultant PT-induced dislocations. As presented in Fig. 9b, the fresh tube first undergoes PT from A to B and the forward PT results in the formation of dislocations in the grain and phase boundaries, developing localized stress concentration. Such processes include E_{B2} , $B2 \rightarrow B19'$ and $E_{B19'}$, showing a typical route of first order stress-induced PT. Then during the unloading stage from B to C, lattice strain was produced, and the dislocations block the reverse PT of nanosized martensite domains. After thousands of cycles in compression, the density of dislocation is almost saturated, and the volume fraction of associated residual martensite reaches a stabilized level. The compressive residual stress is mainly in B2 while the tensile residual stress is in B19'. Upon external compressive loading, the B2 domains under high compressive residual stress can transform to B19' locally even when the external stress is very low. Within the dislocation-wall-separated B2 domains, PT can occur continuously from low stress level to σ_{max} , demonstrating the significant strain hardening behavior from D to E [55]. The reversible PT between D and E can

occur in a stabilized path due to the high compressive residual stress. It is possible for local PT under low external stress and continuous PT is coupled with E_{B2} within the refined domains.

To conclude, the main mechanisms of functional degradation of NiTi tubes are: 1) PT-induced dislocation slip and dislocation-pinned martensite leads to the accumulation of residual strain; 2) the compressive residual stress in the austenite phase results in the reduction of phase transformation stress; 3) the reduction of B2 domain size and internal stress field contribute to the shrinkage of hysteresis loop area.

3.3 Self-enhanced elastocaloric cooling performance

In order to evaluate the elastocaloric performance of NiTi tubes, COP_{mater} and COP of Carnot cycle (COP_{Carnot} , the maximum theoretical efficiency that a thermodynamic cycle can achieve [56]) were measured at different stages during the cyclic compression of the tubes. Fig. 10a presents a thermodynamic cycle, including heat transfer with the air ambient and adiabatic loading/unloading to simulate the heating/cooling process. The temperature profile of the NiTi tubes under forward and reverse PT was captured simultaneously (Fig. 10b). The average temperature of the selected area of the tubes shown by the inset in Fig. 10b is exported and plotted against time. The COP_{mater} can be estimated by Eq. 2 from the input work w ($=D$, as shown in Fig. 10a) and the temperature drop ΔT_c during reverse PT (Fig. 10b).

$$COP_{mater} = \frac{\lambda \cdot \Delta T_c}{w}, \quad (2)$$

where $\lambda = 3.225 \text{ MJ}/(\text{m}^3 \cdot ^\circ\text{C})$ is the specific heat capacity. And the COP_{Carnot} can be

estimated by Eq. 3 from the temperature of the heat source (T_c) and the heat sink (T_h) in a thermodynamic cycle [5, 12, 57, 58].

$$COP_{Carnot} = \frac{T_c}{T_h - T_c}, \quad (3)$$

where T_c and T_h are in Kelvin. Based on the parameters in Fig. 10a-b, it can be evaluated that: $COP_{mater} = 12.65$ and $COP_{Carnot} = 30.39$. The ratio of COP_{mater} to COP_{Carnot} can be seen as the exergetic efficiency evaluating the performance of cooling refrigerant [58, 59].

Based on such evaluation, the evolution of w and ΔT_c was presented in Fig. 10c-d. Detailed thermo-mechanical cycles and temperature profiles can be found in Part 11 of the Supplementary data. w decreased with the increase of N for full PT under 1000 and 1200 MPa. While for the partial PT under 800 MPa, w increased slightly from 2 ($N = 1$) to 3.2 MPa ($N = 10^3$) and then decreased to 2.4 MPa ($N = 10^4$). ΔT_c monotonically decreased as N increased under 1200 MPa, from 15.5 °C to 11.9 °C. Under 1000 MPa, ΔT_c slightly decreased from 13.8 °C to 13.0 °C within 10^4 cycles. Under 800 MPa, ΔT_c initially increased from 6.8 °C to 11.6 °C in the first 10^3 cycles and then slightly dropped to 9.4 °C at $N = 10^4$. The increase in ΔT_c might be ascribed to the decrease in transformation stress and the increase in the amount of PT [16].

Given the evolutions of w and ΔT_c , evolution of COP_{mater} and the exergetic efficiency under various σ_{max} are quantified in Fig. 10e-f. COP_{mater} demonstrates an overall trend of increasing with the increase in N , presenting a self-enhanced behavior. The tube under 800 MPa has the highest COP_{mater} among three stress levels and reaches a maximum value of 12.65 at $N = 10^4$. This advantage maintains throughout the full

range of cyclic compression. For the cases of 1000 and 1200 MPa, COP_{mater} increases monotonically and is almost double at $N=10^4$ compared with that at $N = 1$. As for the exergetic efficiency, a general tendency of improvement is found within 10^3 cycles and then remains above 40% at $N = 10^4$. Under 800 MPa, not only the highest value of COP_{mater} can be achieved but the exergetic efficiency can be improved twice with 10^3 cycles of compression. The origins of such self-enhancement in elastocaloric performance of the NiTi tube under partial PT are due to the increase of ΔT_c . Under full PT, the significant shrinkage of D has a dominant effect on the increase of COP_{mater} . Hence, it is essential to tune the mechanical behaviors via microstructure engineering under suitable stress to minimize the hysteresis loop area (or input work) of NiTi for elastocaloric cooling.

The functional degradation of NiTi generally brings negative effect under real applications, as it demonstrates the unstable cyclic stress-strain responses of NiTi. Nevertheless, the self-enhancement of the elastocaloric cooling performance of NiTi tubes shows that the functional degradation in cyclic σ - ε responses of NiTi is beneficial to the cooling performance. Compared with other SMAs of different shapes [5, 12, 57, 60, 61], NiTi tubes demonstrate a good combination of high COP_{mater} and high specific surface area for efficient heat transfer (Fig. 11). COP_{mater} of the NiTi tube under partial PT at $N=10^4$ even exceeds that of TiNiFe thin film [61], indicating that the NiTi tubes under compression are promising alternatives for elastocaloric cooling.

Furthermore, cyclic compression permits NiTi with self-enhanced cooling performance from partial to full PT. It is also a strategy to create a stable nanostructure

of NiTi with sub-grain defects of dislocation walls and dislocation-pinned residual martensite. The induced defects can significantly decrease the hysteresis loop area and increase COP_{mater} , presenting an effective and simple process to optimize the cooling performance. Introducing defects in NiTi via cyclic compression might be a promising way to fabricate solid-state green refrigerants with tunable COP_{mater} and high cyclic stability. Besides the functional degradation, the study of structural fatigue, optimizations of heat transfer conditions and geometric parameters is under investigation and will be addressed in our future work.

4. Conclusions

Functional degradation and elastocaloric cooling performance of superelastic NiTi tubes are explored under cyclic compressive PT. The following conclusions can be drawn from this study:

- 1) The functional degradation of NiTi tubes under cyclic compression is caused by the PT-induced plasticity, contributed from dislocation slip and residual martensite. The corresponding compressive residual stress in the austenite phase leads to the reduction in forward and reverse PT stress. The dislocation wall partition inside the austenite grains and the internal stress field lead to the shrinkage of hysteresis loop area.
- 2) The elastocaloric cooling performance of the NiTi tubes under cyclic compression is self-enhanced with the increase in cycle number, because of the functional degradation. It is found that the partial PT of NiTi tubes under cyclic

compression is more favorable than full PT for elastocaloric cooling, due to the increases of ΔT_c and COP_{mater} .

- 3) The cyclically-deformed NiTi tube (10^4 cycles of compression under 800 MPa) shows a high COP_{mater} of 12.65. The effective heat transfer structure and high COP_{mater} make NiTi tubes promising materials for green solid-state cooling technology.
- 4) Introducing defects of dislocations and residual martensite in NiTi via cyclic compression might be a helpful processing method to improve cyclic stability and COP_{mater} .

Acknowledgements

This work was financially supported by the Hong Kong Research Grant Council (GRF Project No. 16206119) and the Fundamental Research Program of Shenzhen (Grant No. JCYJ20170412153039309). The authors acknowledge the assistance of Advanced Engineering Materials Facility (AEMF) of HKUST and SUSTech Core Research Facilities. The authors acknowledge Kangjie Chu, Zhongzheng Deng and Qihong Wang for the kind assistance in TEM analysis and mechanical testing.

References

- [1] Y. Cao, X. Zhou, D. Cong, H. Zheng, Y. Cao, Z. Nie, Z. Chen, S. Li, N. Xu, Z. Gao, W. Cai, Y. Wang, Large tunable elastocaloric effect in additively manufactured Ni-Ti shape memory alloys, *Acta Mater.* (2020).
- [2] Y. Shen, Z. Wei, W. Sun, Y. Zhang, E. Liu, J. Liu, Large elastocaloric effect in directionally solidified all-d-metal Heusler metamagnetic shape memory alloys, *Acta Mater.* 188 (2020) 677-685.
- [3] H. Hou, E. Simsek, T. Ma, N.S. Johnson, S. Qian, C. Cissé, D. Stasak, N. Al Hasan, L. Zhou, Y. Hwang, R. Radermacher, V.I. Levitas, M.J. Kramer, M.A. Zaem, A.P. Stebner, R.T. Ott, J. Cui, I.

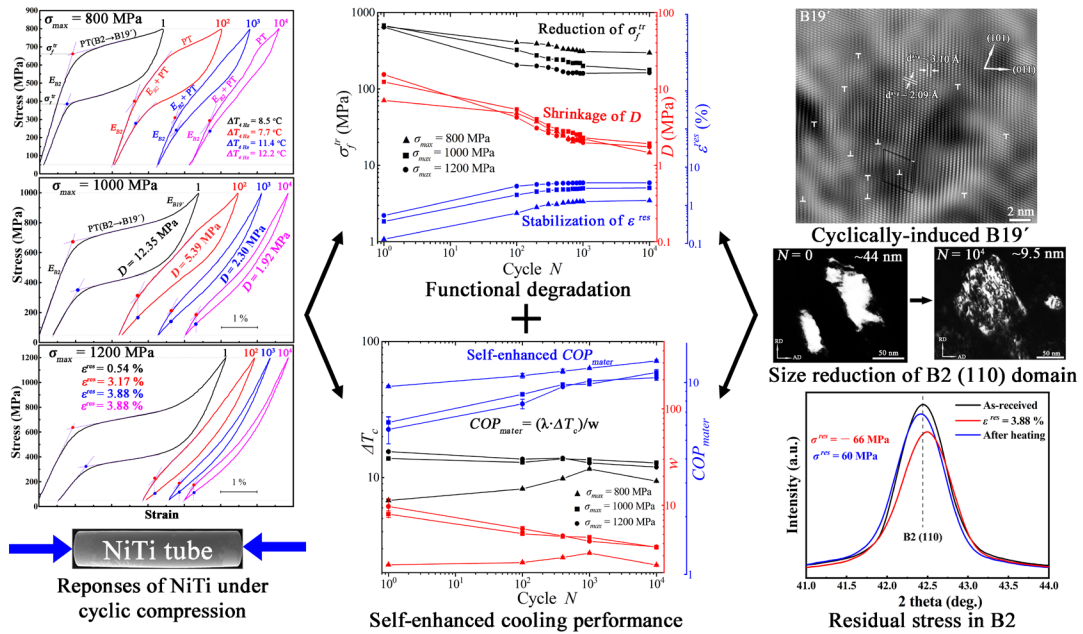
- Takeuchi, Fatigue-resistant high-performance elastocaloric materials made by additive manufacturing, *Science* 366(6469) (2019) 1116.
- [4] Y. Wu, E. Ertekin, H. Sehitoglu, Elastocaloric cooling capacity of shape memory alloys – Role of deformation temperatures, mechanical cycling, stress hysteresis and inhomogeneity of transformation, *Acta Mater.* 135 (2017) 158-176.
- [5] J. Chen, K. Zhang, Q. Kan, H. Yin, Q. Sun, Ultra-high fatigue life of NiTi cylinders for compression-based elastocaloric cooling, *Appl. Phys. Lett.* 115(9) (2019).
- [6] L. Manosa, A. Planes, Materials with Giant Mechanocaloric Effects: Cooling by Strength, *Adv. Mater.* 29(11) (2017).
- [7] H. Sehitoglu, Y. Wu, E. Ertekin, Elastocaloric effects in the extreme, *Scr. Mater.* 148 (2018) 122-126.
- [8] Q.P. Sun, H. Zhao, R. Zhou, D. Saletti, H. Yin, Recent advances in spatiotemporal evolution of thermomechanical fields during the solid–solid phase transition, *Comptes Rendus Mécanique* 340(4-5) (2012) 349-358.
- [9] H. Yin, Q. Sun, Temperature Variation in NiTi Shape Memory Alloy During Cyclic Phase Transition, *J. Mater. Eng. Perform.* 21(12) (2012) 2505-2508.
- [10] J. Tušek, K. Engelbrecht, D. Eriksen, S. Dall’Olio, J. Tušek, N. Pryds, A regenerative elastocaloric heat pump, *Nature Energy* 1(10) (2016).
- [11] H. Ossmer, F. Lambrecht, M. Gültig, C. Chluba, E. Quandt, M. Kohl, Evolution of temperature profiles in TiNi films for elastocaloric cooling, *Acta Mater.* 81 (2014) 9-20.
- [12] J. Cui, Y. Wu, J. Muehlbauer, Y. Hwang, R. Radermacher, S. Fackler, M. Wuttig, I. Takeuchi, Demonstration of high efficiency elastocaloric cooling with large ΔT using NiTi wires, *Appl. Phys. Lett.* 101(7) (2012).
- [13] J. Tušek, K. Engelbrecht, L.P. Mikkelsen, N. Pryds, Elastocaloric effect of Ni-Ti wire for application in a cooling device, *J. Appl. Phys.* 117(12) (2015).
- [14] J. Tušek, A. Žerovnik, M. Čebren, M. Brojan, B. Žužek, K. Engelbrecht, A. Cadelli, Elastocaloric effect vs fatigue life: Exploring the durability limits of Ni-Ti plates under pre-strain conditions for elastocaloric cooling, *Acta Mater.* 150 (2018) 295-307.
- [15] G.J. Pataky, E. Ertekin, H. Sehitoglu, Elastocaloric cooling potential of NiTi, Ni₂FeGa, and CoNiAl, *Acta Mater.* 96 (2015) 420-427.
- [16] K. Zhang, G. Kang, Q. Sun, High fatigue life and cooling efficiency of NiTi shape memory alloy under cyclic compression, *Scr. Mater.* 159 (2019) 62-67.
- [17] H. Hou, J. Cui, S. Qian, D. Catalini, Y. Hwang, R. Radermacher, I. Takeuchi, Overcoming fatigue through compression for advanced elastocaloric cooling, *MRS Bulletin* 43(4) (2018) 285-290.
- [18] S. Qian, Y. Geng, Y. Wang, J. Ling, Y. Hwang, R. Radermacher, I. Takeuchi, J. Cui, A review of elastocaloric cooling: Materials, cycles and system integrations, *Int. J. Refrig.* 64 (2016) 1-19.
- [19] S. Qian, A. Alabdulkarem, J. Ling, J. Muehlbauer, Y. Hwang, R. Radermacher, I. Takeuchi, Performance enhancement of a compressive thermoelastic cooling system using multi-objective optimization and novel designs, *Int. J. Refrig.* 57 (2015) 62-76.
- [20] L. Porenta, P. Kabirifar, A. Žerovnik, M. Čebren, B. Žužek, M. Dolenc, M. Brojan, J. Tušek, Thin-walled Ni-Ti tubes under compression: ideal candidates for efficient and fatigue-resistant elastocaloric cooling, *Appl. Mater. Today* 20 (2020).
- [21] S.-M. Kirsch, F. Welsch, N. Michaelis, M. Schmidt, A. Wiczorek, J. Frenzel, G. Eggeler, A. Schütze, S. Seelecke, NiTi-Based Elastocaloric Cooling on the Macroscale: From Basic Concepts to Realization, *Energy Tech.* 6(8) (2018) 1567-1587.

- [22] G. Scire` Mammano, E. Dragoni, Functional fatigue of Ni–Ti shape memory wires under various loading conditions, *Int. J. Fatigue* 69 (2014) 71-83.
- [23] P. Sedm`k, P. Šittner, J. Pilch, C. Curfs, Instability of cyclic superelastic deformation of NiTi investigated by synchrotron X-ray diffraction, *Acta Mater.* 94 (2015) 257-270.
- [24] G. Eggeler, E. Hornbogen, A. Yawny, A. Heckmann, M. Wagner, Structural and functional fatigue of NiTi shape memory alloys, *Mater. Sci. Eng., A* 378(1-2) (2004) 24-33.
- [25] Y. Gao, L. Casalena, M.L. Bowers, R.D. Noebe, M.J. Mills, Y. Wang, An origin of functional fatigue of shape memory alloys, *Acta Mater.* 126 (2017) 389-400.
- [26] H. Soul, A. Isalgue, A. Yawny, V. Torra, F.C. Lovey, Pseudoelastic fatigue of NiTi wires: frequency and size effects on damping capacity, *Smart Mater. Struct.* 19(8) (2010) 085006.
- [27] D.A. Miller, D.C. Lagoudas, Thermomechanical characterization of NiTiCu and NiTi SMA actuators: influence of plastic strains, *Smart Mater. Struct.* 9(5) (2000) 640-652.
- [28] K. Otsuka, X. Ren, Physical metallurgy of Ti–Ni-based shape memory alloys, *Prog. Mater. Sci* 50(5) (2005) 511-678.
- [29] P. Hua, K. Chu, F. Ren, Q. Sun, Cyclic phase transformation behavior of nanocrystalline NiTi at microscale, *Acta Mater.* 185 (2020) 507-517.
- [30] J. Frenzel, G. Eggeler, E. Quandt, S. Seelecke, M. Kohl, High-performance elastocaloric materials for the engineering of bulk- and micro-cooling devices, *MRS Bulletin* 43(4) (2018) 280-284.
- [31] C. Chluba, W. Ge, R. Lima de Miranda, J. Strobel, L. Kienle, E. Quandt, M. Wuttig, Ultralow-fatigue shape memory alloy films, *Science* 348(6238) (2015) 1004.
- [32] M. Wagner, T. Sawaguchi, G. Kaustr`ter, D. H`ffken, G. Eggeler, Structural fatigue of pseudoelastic NiTi shape memory wires, *Mater. Sci. Eng., A* 378(1-2) (2004) 105-109.
- [33] Z. Xie, Y. Liu, J. Van Humbeeck, Microstructure of NiTi shape memory alloy due to tension–compression cyclic deformation, *Acta Mater.* 46(6) (1998) 1989-2000.
- [34] K. Gall, H.J. Maier, Cyclic deformation mechanisms in precipitated NiTi shape memory alloys, *Acta Mater.* 50(18) (2002) 4643-4657.
- [35] R.F. Hamilton, H. Sehitoglu, Y. Chumlyakov, H.J. Maier, Stress dependence of the hysteresis in single crystal NiTi alloys, *Acta Mater.* 52(11) (2004) 3383-3402.
- [36] A. Ahadi, Q. Sun, Stress hysteresis and temperature dependence of phase transition stress in nanostructured NiTi—Effects of grain size, *Appl. Phys. Lett.* 103(2) (2013).
- [37] E. Bonnot, R. Romero, L. Manosa, E. Vives, A. Planes, Elastocaloric effect associated with the martensitic transition in shape-memory alloys, *Phys. Rev. Lett.* 100(12) (2008) 125901.
- [38] L. Mañosa, S. Jarque-Farnos, E. Vives, A. Planes, Large temperature span and giant refrigerant capacity in elastocaloric Cu–Zn–Al shape memory alloys, *Appl. Phys. Lett.* 103(21) (2013).
- [39] C. Yu, G. Kang, D. Song, Q. Kan, Effect of martensite reorientation and reorientation-induced plasticity on multiaxial transformation ratchetting of super-elastic NiTi shape memory alloy: New consideration in constitutive model, *Int J Plasticity* 67 (2015) 69-101.
- [40] Y. Liu, D. Favier, Stabilisation of martensite due to shear deformation via variant reorientation in polycrystalline NiTi, *Acta Mater.* 48(13) (2000) 3489-3499.
- [41] P. Šittner, L. Heller, J. Pilch, C. Curfs, T. Alonso, D. Favier, Young’s Modulus of Austenite and Martensite Phases in Superelastic NiTi Wires, *J. Mater. Eng. Perform.* 23(7) (2014) 2303-2314.
- [42] H. Yin, Y. He, Q. Sun, Effect of deformation frequency on temperature and stress oscillations in cyclic phase transition of NiTi shape memory alloy, *J. Mech. Phys. Solids* 67 (2014) 100-128.
- [43] J. Lim, D. McDowell, Degradation of an Ni-Ti alloy during cyclic loading, *SPIE*1994.

- [44] C. Maletta, E. Sgambitterra, F. Furgiuele, R. Casati, A. Tuissi, Fatigue of pseudoelastic NiTi within the stress-induced transformation regime: a modified Coffin–Manson approach, *Smart Mater. Struct.* 21(11) (2012).
- [45] J. Pfetzinger-Micklich, R. Ghisleni, T. Simon, C. Somsen, J. Michler, G. Eggeler, Orientation dependence of stress-induced phase transformation and dislocation plasticity in NiTi shape memory alloys on the micro scale, *Mater. Sci. Eng., A* 538 (2012) 265-271.
- [46] B. Ye, B.S. Majumdar, I. Dutta, Texture development and strain hysteresis in a NiTi shape-memory alloy during thermal cycling under load, *Acta Mater.* 57(8) (2009) 2403-2417.
- [47] A. Ahadi, Q. Sun, Stress-induced nanoscale phase transition in superelastic NiTi by in situ X-ray diffraction, *Acta Mater.* 90 (2015) 272-281.
- [48] X.B. Shi, F.M. Guo, J.S. Zhang, H.L. Ding, L.S. Cui, Grain size effect on stress hysteresis of nanocrystalline NiTi alloys, *J. Alloys Compd.* 688 (2016) 62-68.
- [49] J. Koike, D.M. Parkin, M. Nastasi, Crystal-to-amorphous transformation of NiTi induced by cold rolling, *J. Mater. Res.* 5(7) (2011) 1414-1418.
- [50] P. Šittner, P. Sedlák, H. Seiner, P. Sedmák, J. Pilch, R. Delville, L. Heller, L. Kadeřávek, On the coupling between martensitic transformation and plasticity in NiTi: Experiments and continuum based modelling, *Prog. Mater. Sci.* 98 (2018) 249-298.
- [51] E.J.V.J.S. Grüneisen, Berlin, *Handbuch der Physik*, (1926).
- [52] K. Tsuchiya, M. Inuzuka, D. Tomus, A. Hosokawa, H. Nakayama, K. Morii, Y. Todaka, M. Umemoto, Martensitic transformation in nanostructured TiNi shape memory alloy formed via severe plastic deformation, *Mater. Sci. Eng., A* 438-440 (2006) 643-648.
- [53] H. Chen, Y.-D. Wang, Z. Nie, R. Li, D. Cong, W. Liu, F. Ye, Y. Liu, P. Cao, F. Tian, X. Shen, R. Yu, L. Vitos, M. Zhang, S. Li, X. Zhang, H. Zheng, J.F. Mitchell, Y. Ren, Unprecedented non-hysteretic superelasticity of [001]-oriented NiCoFeGa single crystals, *Nat. Mater.* (2020).
- [54] M.F.X. Wagner, N. Nayan, U. Ramamurty, Healing of fatigue damage in NiTi shape memory alloys, *J. Phys. D: Appl. Phys.* 41(18) (2008) 185408.
- [55] H. Mughrabi, Dislocation wall and cell structures and long-range internal stresses in deformed metal crystals, *Acta Metall.* 31(9) (1983) 1367-1379.
- [56] S. Qian, D. Nasuta, A. Rhoads, Y. Wang, Y. Geng, Y. Hwang, R. Radermacher, I. Takeuchi, Not-in-kind cooling technologies: A quantitative comparison of refrigerants and system performance, *Int. J. Refrig.* 62 (2016) 177-192.
- [57] H. Hou, E. Simsek, D. Stasak, N.A. Hasan, S. Qian, R. Ott, J. Cui, I. Takeuchi, Elastocaloric cooling of additive manufactured shape memory alloys with large latent heat, *J. Phys. D: Appl. Phys.* 50(40) (2017).
- [58] S. Qian, J. Ling, Y. Hwang, R. Radermacher, I. Takeuchi, Thermodynamics cycle analysis and numerical modeling of thermoelastic cooling systems, *Int. J. Refrig.* 56 (2015) 65-80.
- [59] J. Steven Brown, P.A. Domanski, Review of alternative cooling technologies, *Appl. Thermal Eng.* 64(1-2) (2014) 252-262.
- [60] Y. Kim, M.-G. Jo, J.-W. Park, H.-K. Park, H.N. Han, Elastocaloric effect in polycrystalline Ni 50 Ti 45.3 V 4.7 shape memory alloy, *Scr. Mater.* 144 (2018) 48-51.
- [61] H. Ossmer, F. Wendler, M. Gueltig, F. Lambrecht, S. Miyazaki, M. Kohl, Energy-efficient miniature-scale heat pumping based on shape memory alloys, *Smart Mater. Struct.* 25(8) (2016).

Functional Degradation and Self-enhanced Elastocaloric Cooling

Performance of NiTi Tubes under Cyclic Compression



Graphical abstract

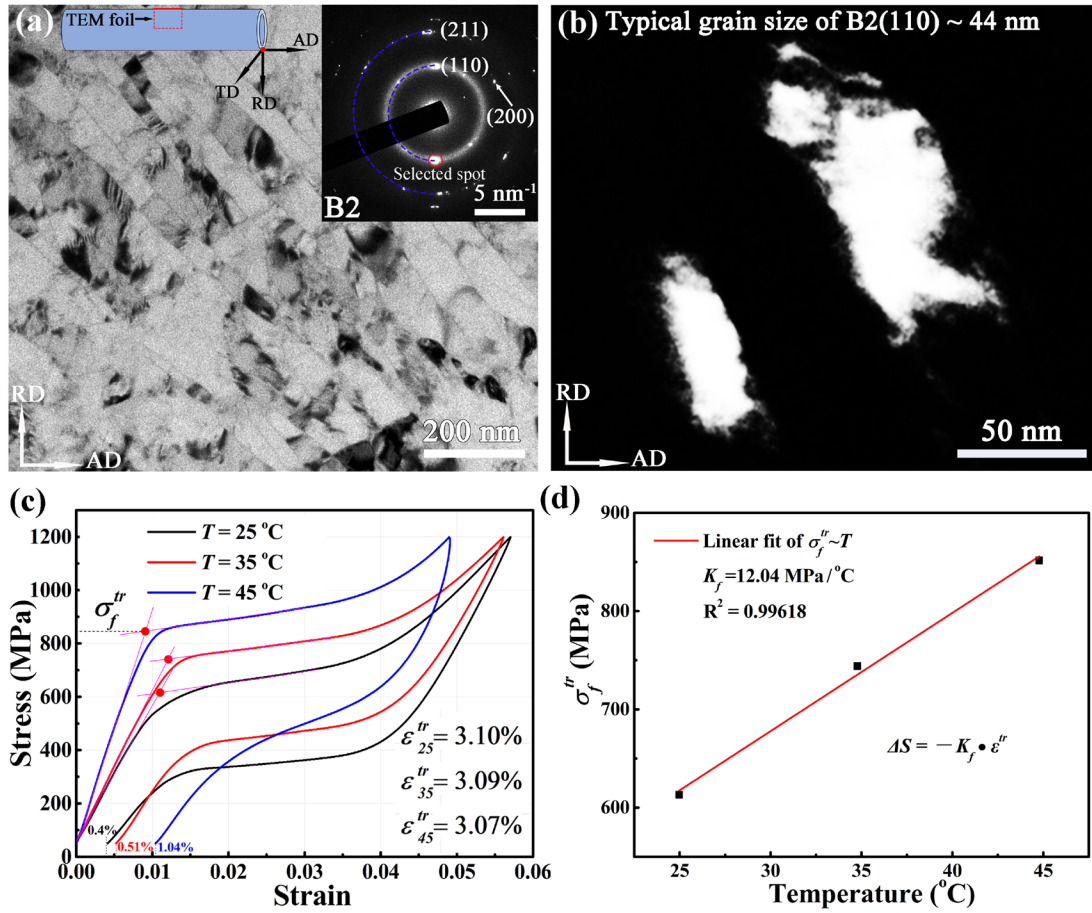


Fig. 1. (a) Bright field TEM image of as received NiTi tube with radial direction (RD) and axial direction (AD) labelled; (b) dark field TEM image taken with the diffraction spot of B2 (110); (c) isothermal compressive $\sigma\sim\varepsilon$ responses of NiTi tubes at 25, 35 and 45 °C; (d) temperature dependence of the forward transformation stress σ_f^{tr} .

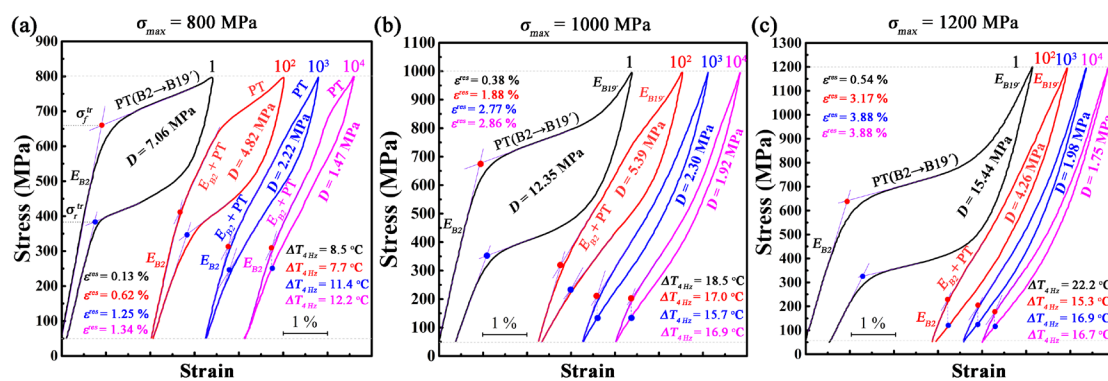


Fig. 2. Evolution of isothermal compressive $\sigma\sim\varepsilon$ responses under (a) $\sigma_{max} = 800$ MPa, (b) $\sigma_{max} = 1000$ MPa and (c) $\sigma_{max} = 1200$ MPa.

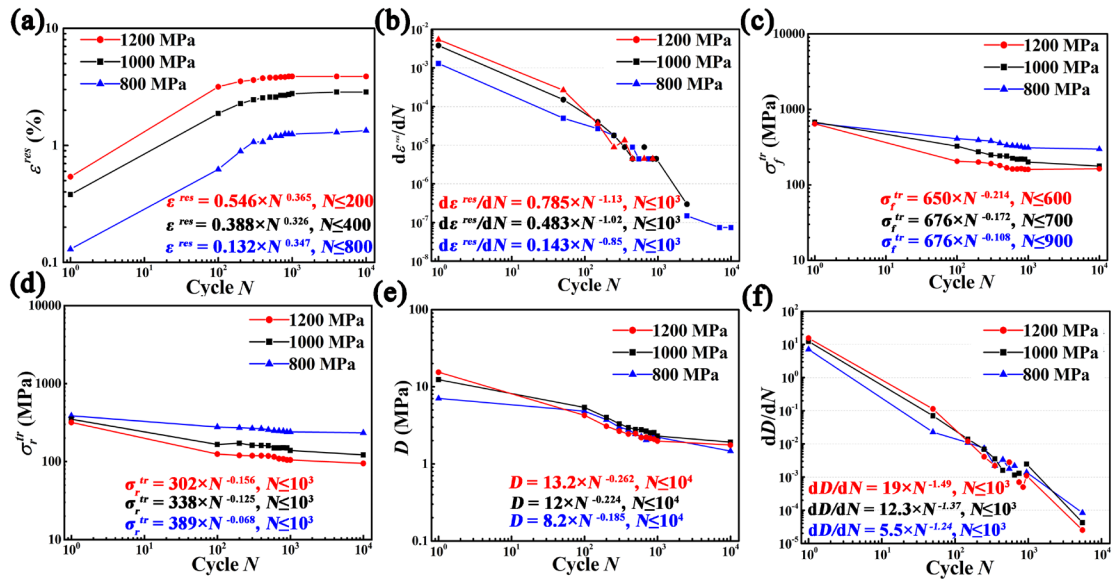


Fig. 3. Functional degradation of the NiTi tube under different stress levels as characterized by (a) $\varepsilon^{res} \sim N$ and (b) $d\varepsilon^{res}/dN \sim N$; (c) $\sigma_f^{tr} \sim N$ and (d) $\sigma_r^{tr} \sim N$; (e) $D \sim N$ and (f) $dD/dN \sim N$.

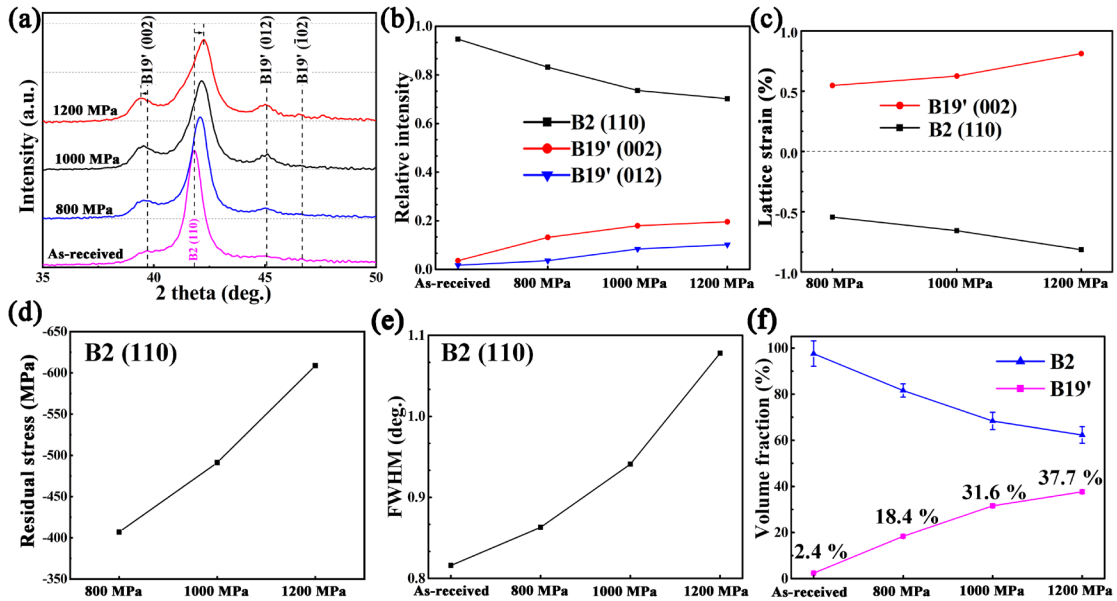


Fig. 4. (a) XRD patterns of cyclically-deformed tubes after 10^4 cycles under 800 MPa, 1000 and 1200 MPa; (b) relative intensity of diffraction peaks of B2 and B19'; (c) lattice strain; (d) residual stress in austenite B2 (110) at $N=10^4$ versus σ_{max} ; (e) FWHM of B2(110); (f) volume fraction of B2 and B19' estimated via Rietveld refinement.

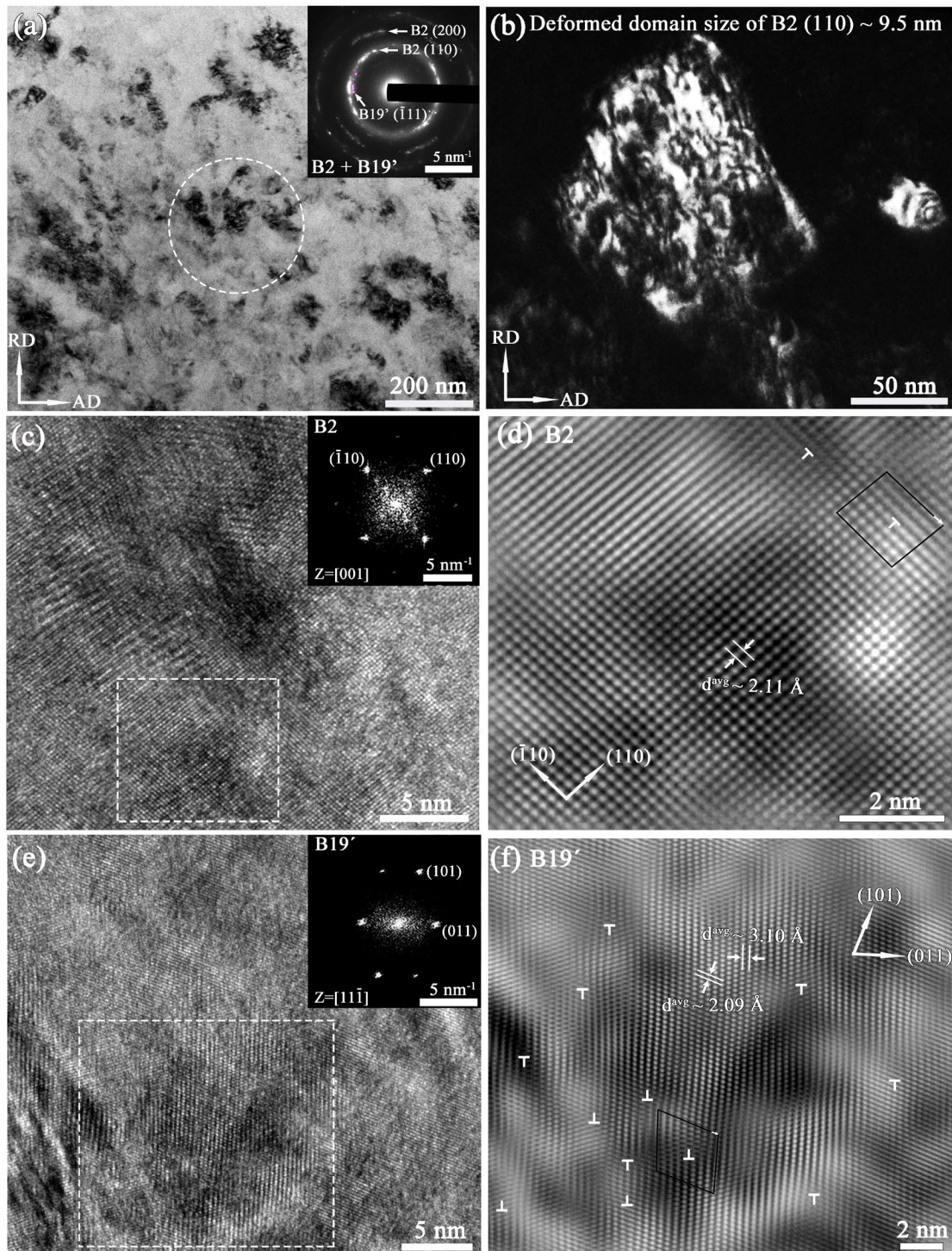


Fig. 5. Cyclically-deformed microstructure after 10^4 cycles under 1200 MPa. (a) The bright field TEM image with SADP (inset); (b) the dark field TEM image taken with the diffraction spot of B2 (110); (c) the high resolution TEM image of B2 austenite; (d) the inverse fast Fourier transformation (IFFT) image from the selected area in (c); (e) the high resolution TEM image of B19' martensite; (d) the IFFT image from the selected area in (e).

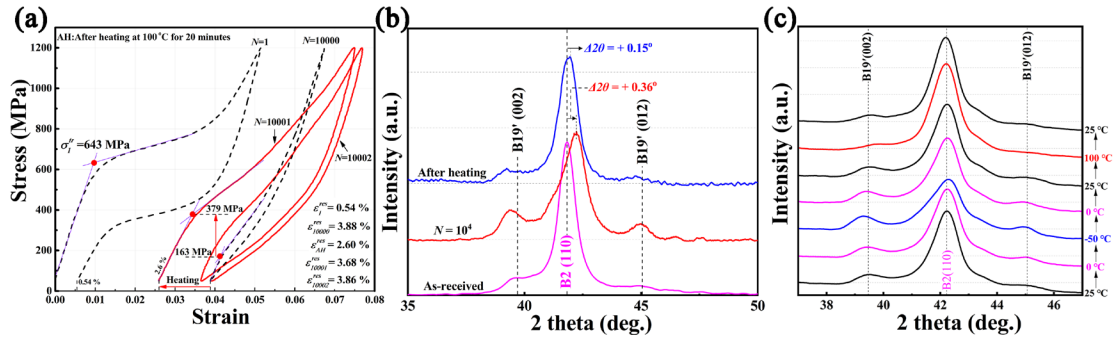


Fig. 6. (a) Comparison of isothermal σ - ϵ responses among $N = 1$, $N = 10^4$, $N = 10001$ and $N = 10002$ (tested after heating at 100 °C for 20 minutes); (b) comparison of XRD patterns of the as-received tube, the tube after 10^4 cycles of compression under $\sigma_{max}=1200$ MPa and the tube after heating at 100 °C for 20 minutes; (c) *in situ* XRD patterns of the deformed tube ($N=2\times 10^4$, $\epsilon^{res} = 3.88\%$).

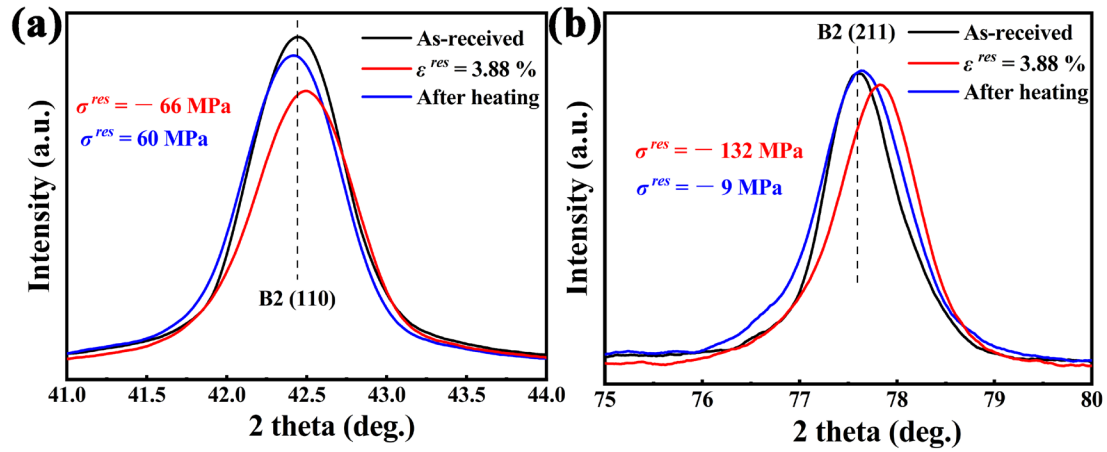


Fig. 7. XRD patterns of as-received tube, the deformed tube ($N=2\times 10^4$, $\epsilon^{res} = 3.88\%$) and the deformed tube after heating along the loading direction. (a) B2 (110); (b) B2 (211)

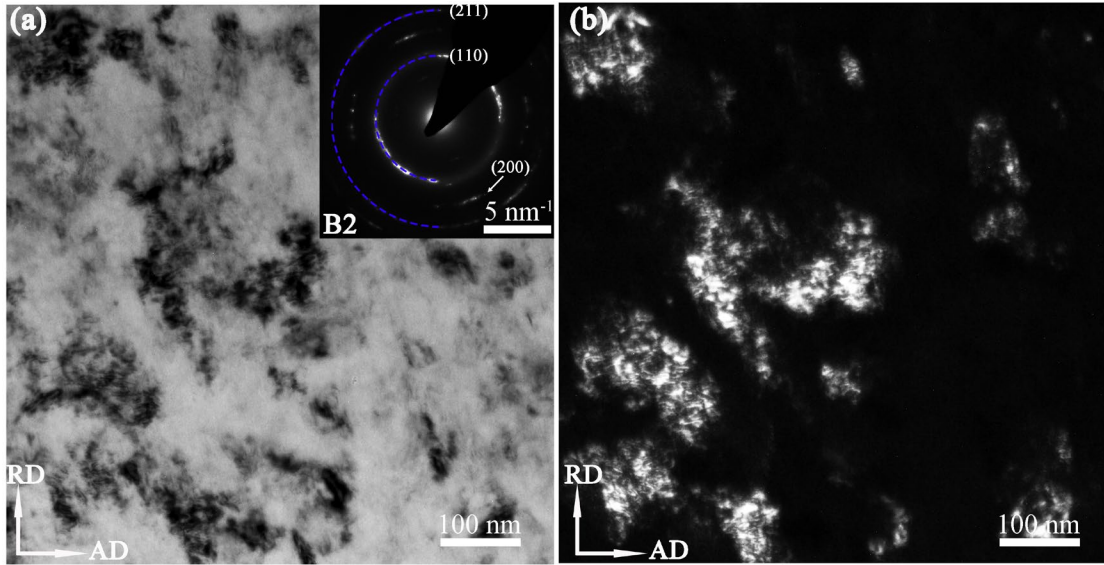


Fig. 8. Microstructure of the cyclically-deformed tube after heating at 100 °C for 20 minutes. (a) The bright field TEM image with the selected area diffraction pattern; (b) the dark field TEM image taken with the diffraction spot of B2 (110).

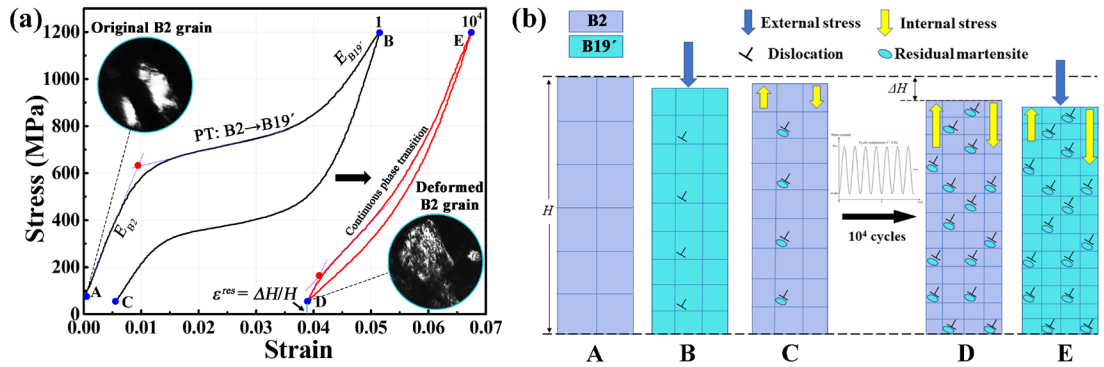


Fig. 9 (a) Isothermal $\sigma\sim\varepsilon$ responses at $N=1$ and $N=10^4$; (b) schematic illustration of the stabilization mechanism of the NiTi tube under cyclic compression.

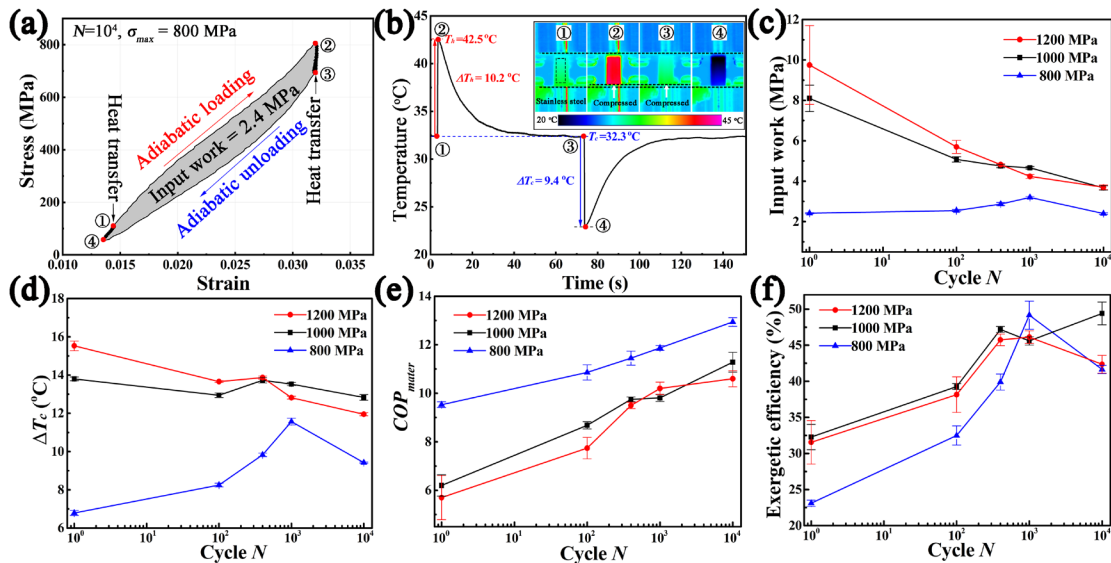


Fig. 10 Self-enhancement of elastocaloric cooling under different stress levels. (a) the mechanical $\sigma\sim\varepsilon$ response of COP measurement under $\sigma_{max} = 800$ MPa at $N=10^4$; (b) *in situ* detected temperature profile; evolution of input work (c), adiabatic cooling temperature drop (d), COP_{mater} (e) and exergetic efficiency (d).

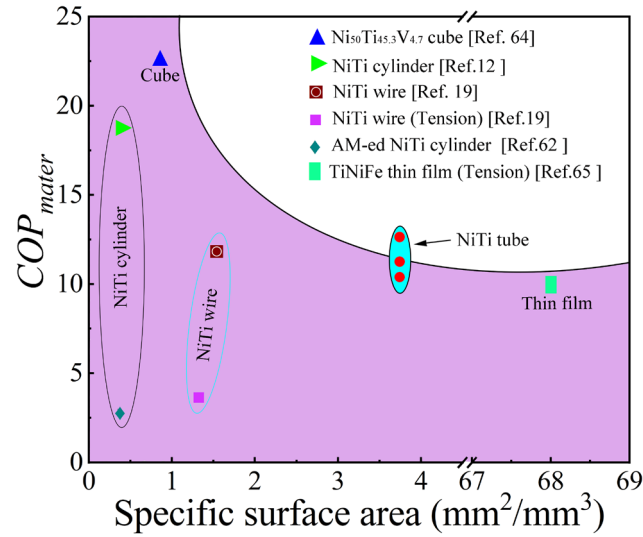


Fig. 11 Comparison of specific surface area and COP_{mater} for NiTi tube and other NiTi based SMAs.

Supplementary Materials

Functional Degradation and Self-enhanced Elastocaloric Cooling Performance of NiTi Tubes under Cyclic Compression

Dingshan Liang^{1,2}, Peng Hua¹, Junyu Chen³, Fuzeng Ren^{2,*}, Qingping Sun^{1,*}

¹ Department of Mechanical and Aerospace Engineering, The Hong Kong University of Science and Technology, Clear Water Bay, Kowloon, Hong Kong, China

² Department of Materials Science and Engineering, Southern University of Science and Technology, Shenzhen, Guangdong, China

³ Department of Engineering Mechanics, School of Civil Engineering, Wuhan University, Wuhan, Hubei, China

Corresponding Author. E-mail: renfz@sustech.edu.cn; meqpsun@ust.hk

Keywords: Elastocaloric cooling; Cyclic response; NiTi; Shape memory alloy (SMA); Martensitic phase transformation.

1. Determination of austenite finish temperature

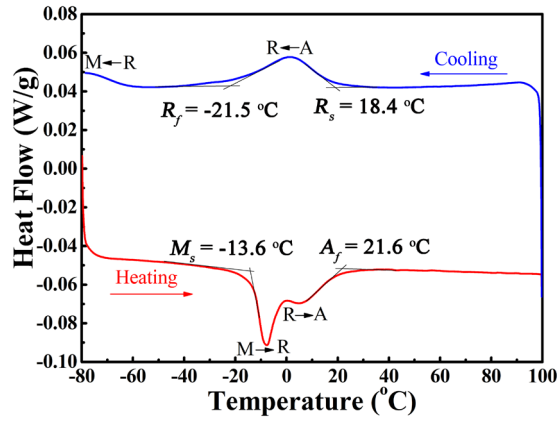


Fig. S1. Differential scanning calorimetry curves of the NiTi tube ranging from $-80\text{ }^\circ\text{C}$ to $100\text{ }^\circ\text{C}$.

2. Experimental set-up

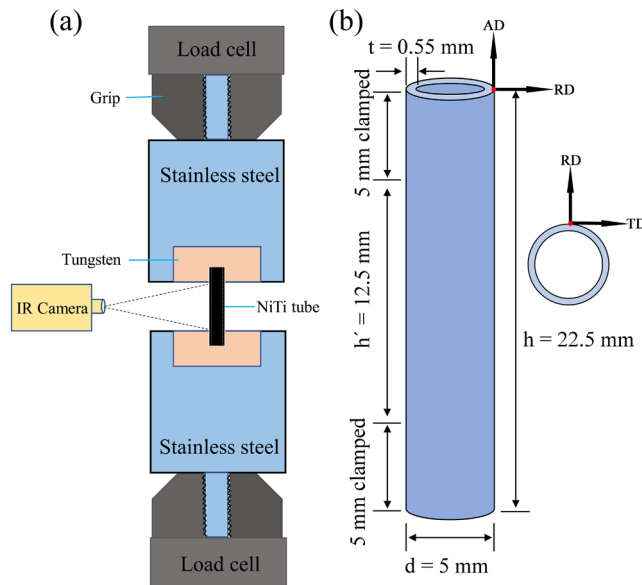


Fig. S2. (a) Schematic illustration of the designed clamping compression fixture for NiTi tubes; (b) Geometrical dimensions of NiTi tubes with an effective height (h') of 12.5 mm . The radial direction, axial direction and tangential direction of NiTi tubes were denoted as RD, AD and TD, respectively.

3. Estimation of buckling

The elastic buckling of solid structure subjected to clamping conditions can be estimated by

$$P_{cr} = \frac{4\pi^2 EI}{l^2} \quad (1)$$

where P_{cr} is the critical load, E is the elastic modulus, I is the second momentum of inertia, l is the length [1]. However, the elastic modulus of superelastic NiTi is highly temperature-sensitive and the slope of strain-stress curve during phase transformation region is very small. That is, the NiTi tube might not be buckled at the elastic region but easily buckled at the PT region. To be more conservative, take the slope of PT region during isothermal strain-stress curve at 25 °C as E_{PT} , substituting the elastic modulus in equation (1). For NiTi tube with outer diameter of 5 mm and inner diameter of 3.9 mm: the maximum applied stress P_{cr} is 1200 MPa; E_{PT} is 4285 MPa from Fig. 1(c) ; I is 19.32 mm⁴. So, the maximum allowed length l_{max} is 18.819 mm. In the clamping head as showed in Fig. S2, the effective length of the tube is 12.5 mm, which is smaller than the l_{max} . Therefore, the tube will not buckle under such clamping condition.

4. Monoclinic compression test

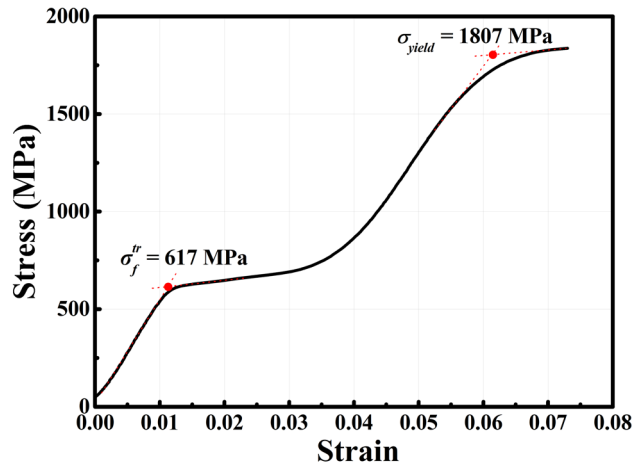


Fig. S3. Monotonic compression of NiTi tubes subjected to plastic deformation at room temperature.

5. Temperature drop under 800 MPa

As shown in Fig. S4a, the tube was loaded to 800 MPa slowly and held the force to attain a maximum strain, then adiabatically unloaded in 0.2 S to get a temperature drop.

Fig. S4b shows the temperature was first increased to about 35 °C and then cooled back to near the level of room temperature. An adiabatic temperature drop of 25 °C was observed during the unloading process.

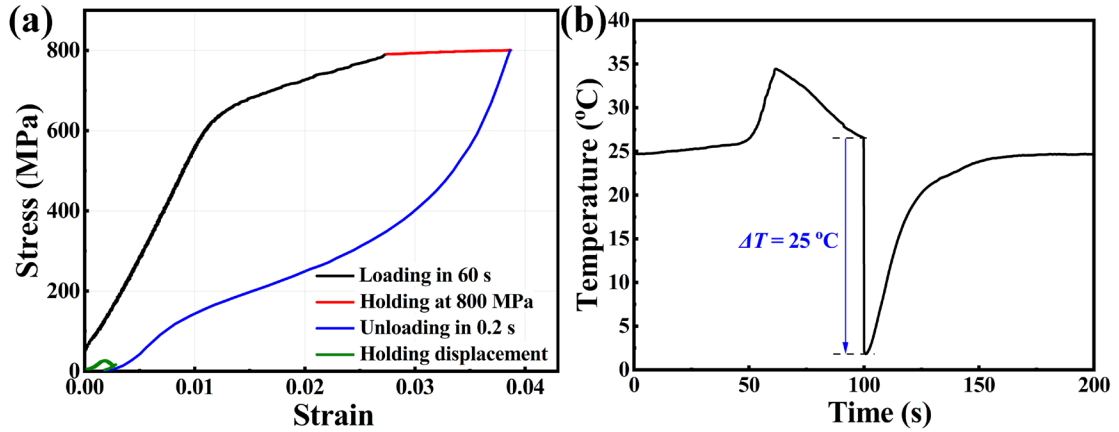


Fig. S4. (a) Mechanical stress-strain response of the measurement of maximum temperature drop; (b) *in situ* temperature profile with a temperature drop of 25 °C.

6. Evolution of 4 Hz cyclic compression

In contrast to the isothermal response tested after certain cycles of compression, the cyclic compression at 4 Hz was conducted to accumulate cycle number N continuously within a period. The first, 100th, 1000th and 10000th cycle in the cyclic compression with *in situ* detected temperature profile were presented in Fig. S5 to characterize the evolutions coupling with heat generation (forward phase transition and hysteresis heat) and absorption (reverse phase transition) under various σ_{max} .

Under σ_{max} of 800 MPa, the shape of strain-stress curve involves from a top-right broad “leaf” with residual strain at the beginning to a slim “needle” sharpening at both end after 10⁴ cycles (Fig. S5a). As a result, the amplitude of temperature oscillation (ΔT) first drops from 8.5 °C to 7.7 °C for the first 100 cycles of compression, and then gradually improves to 11.4 °C at $N=10^3$ and 12.2 °C at $N=10^4$ (Fig. S5b). As the cycles accumulated, the faster the temperature rises versus time (Fig. S5c). These can be related to the decrease of σ_f^{tr} , so the temperature rises quickly at the low stress level. Not that the maximum stress was achieved at $t = 0.125s$.

Under σ_{max} of 1000 MPa and 1200 MPa, the shape of σ - ε curves both change from middle-wide open loops to slim sickle-like types with oblivious hardening in the up-right ends (Fig. S5d&g). The obvious hardening at the stage of elastic deformation is mainly due to the preferred orientation of stress-induced martensite along the loading direction possessing high modulus [2]. The hysteresis loop area shrinks first from 4.18 MPa at the beginning to 1.72 MPa at $N=100$ and stabilizes to 1.63 MPa after 10^3 cycles under $\sigma_{max} = 1000$ MPa. While it keeps decreasing non-monotonically from 7.47 MPa at the beginning to 1.49 MPa at $N=10^4$ for the case under σ_{max} of 1200 MPa. The reversible strain behaves like ΔT under $\sigma_{max} = 1000$ MPa, both demonstrating a reduction first from the beginning to $N=100$ and then a gradual increase till $N=10^4$. The time dependence of temperature is similar as that under $\sigma_{max} = 800$ MPa, showing the more cycles compressed the quicker temperature rises. Under $\sigma_{max} = 1200$ MPa, the reversible strain manifests a rapid reduction from 3.4% to 2.6% during the first 100 cycles and then evolves very slowly to 2.5% and 2.4% for $N = 10^3$ and $N=10^4$ (Fig. S5e). As for the temperature oscillation, it first drops from 22.2 °C to 15.3 °C for the first 100 cycles, then rises to about 16.9 °C at $N = 10^3$, and final decreases slowly (Fig. S5i). The time dependence of temperature is not obvious under $\sigma_{max} = 1200$ MPa. This might be ascribed to the coupling of latent heat release and hysteresis heat. For the first cycle, it is notable that the temperature at $t = 0.25$ s cannot fall back to the same level at $t = 0$ s, displaying a gap proportional to the maximum applied stress (Fig. S5b,e&h). This should be accredited to the continuous release of hysteresis heat during unloading.

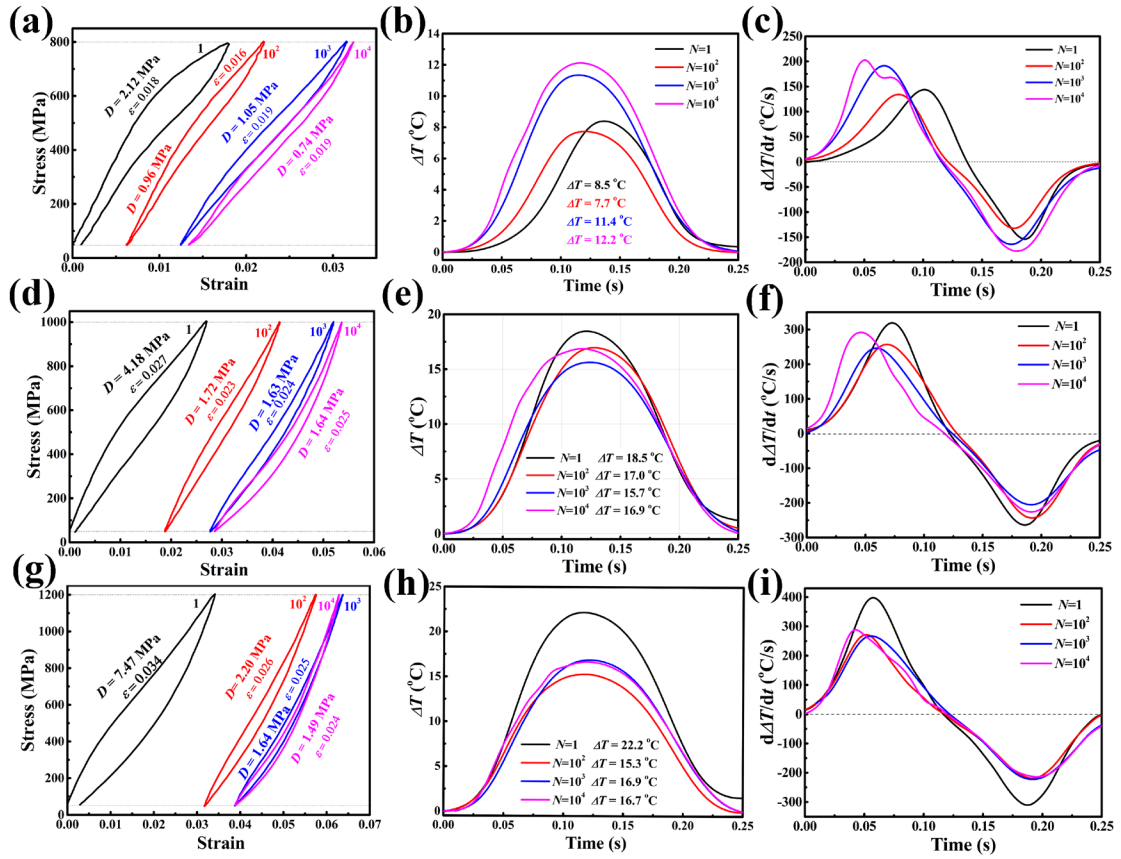


Fig. S5. Mechanical evolution of 4 Hz cyclic compression under (a) $\sigma_{max} = 800$ MPa, (d) $\sigma_{max} = 1000$ MPa and (g) $\sigma_{max} = 1200$ MPa; *In situ* temperature profile as a function of time under (b) $\sigma_{max} = 800$ MPa, (e) $\sigma_{max} = 1000$ MPa and (h) $\sigma_{max} = 1200$ MPa; $d\Delta T/dt$ as a function of time under (c) $\sigma_{max} = 800$ MPa, (f) $\sigma_{max} = 1000$ MPa and (i) $\sigma_{max} = 1200$ MPa.

7. Rietveld refinement via MAUD

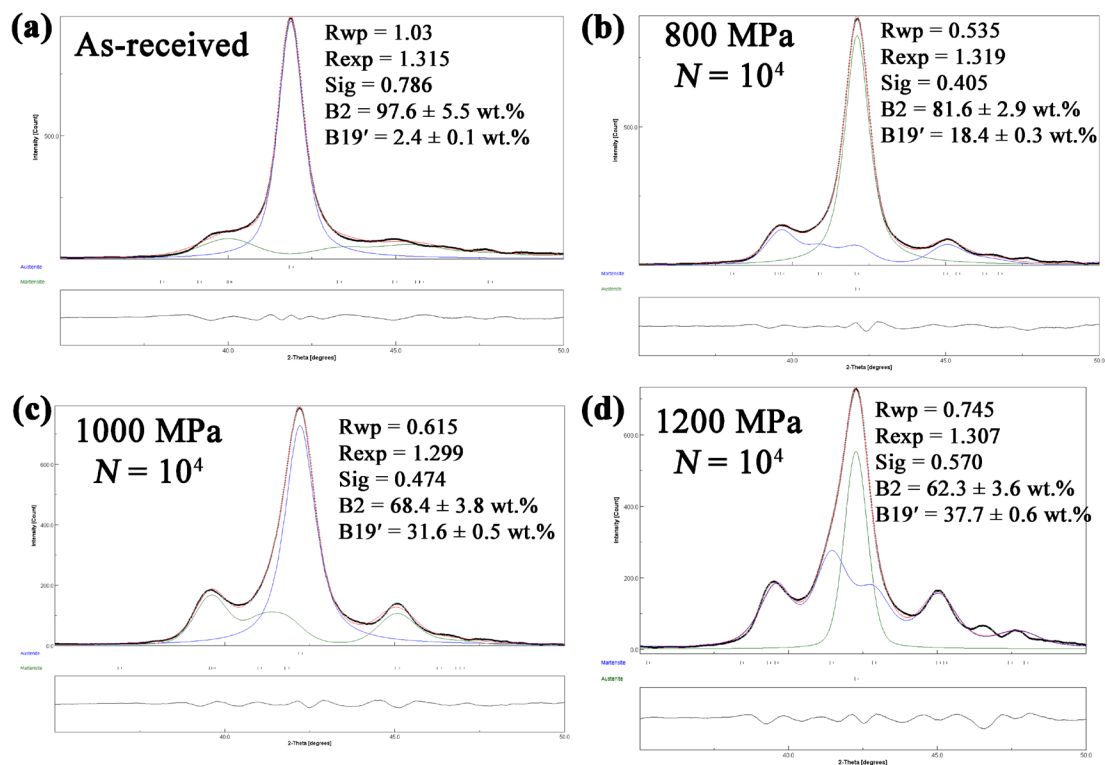


Fig. S6. Rietveld refinement analysis of the XRD patterns obtained from the tube surface of (a) as-received, cyclically-deformed under 800 MPa (b), 1000 MPa (c) and 1200 MPa (d) tubes.

8. Surface morphologies evolution

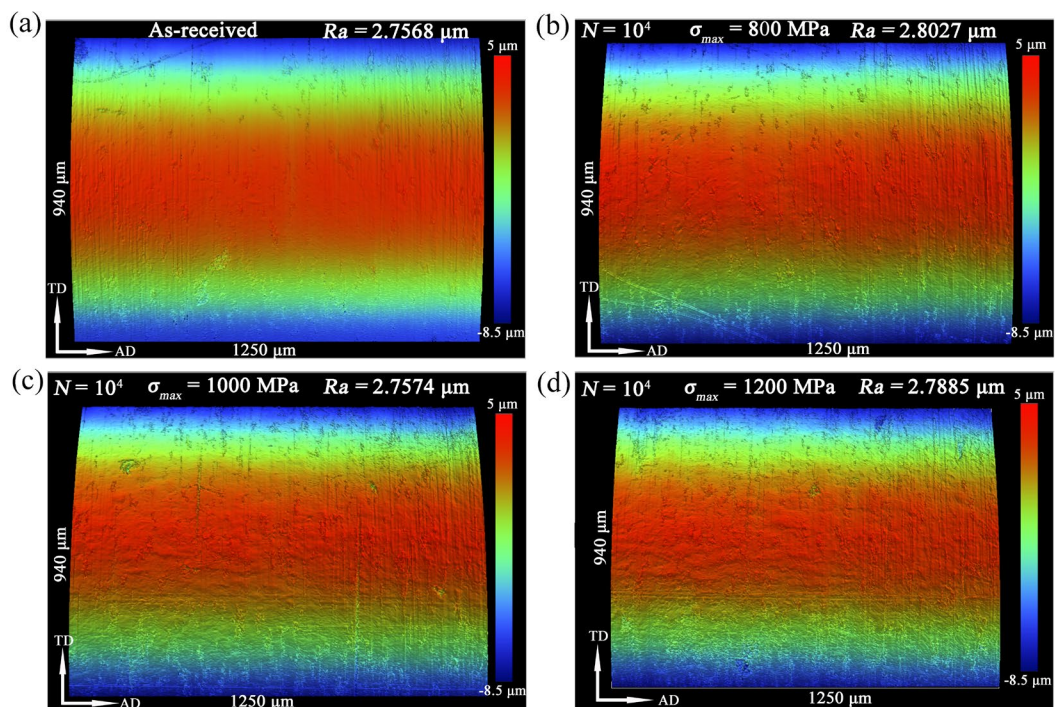


Fig. S7. 3D surface profiles of as-received tubes and cyclically-deformed tubes.

The increased surface roughness (Ra) of the cyclically-deformed tubes should be a result of phase-transformation induced plasticity.

9. Residual lattice strain in B2 via SAED

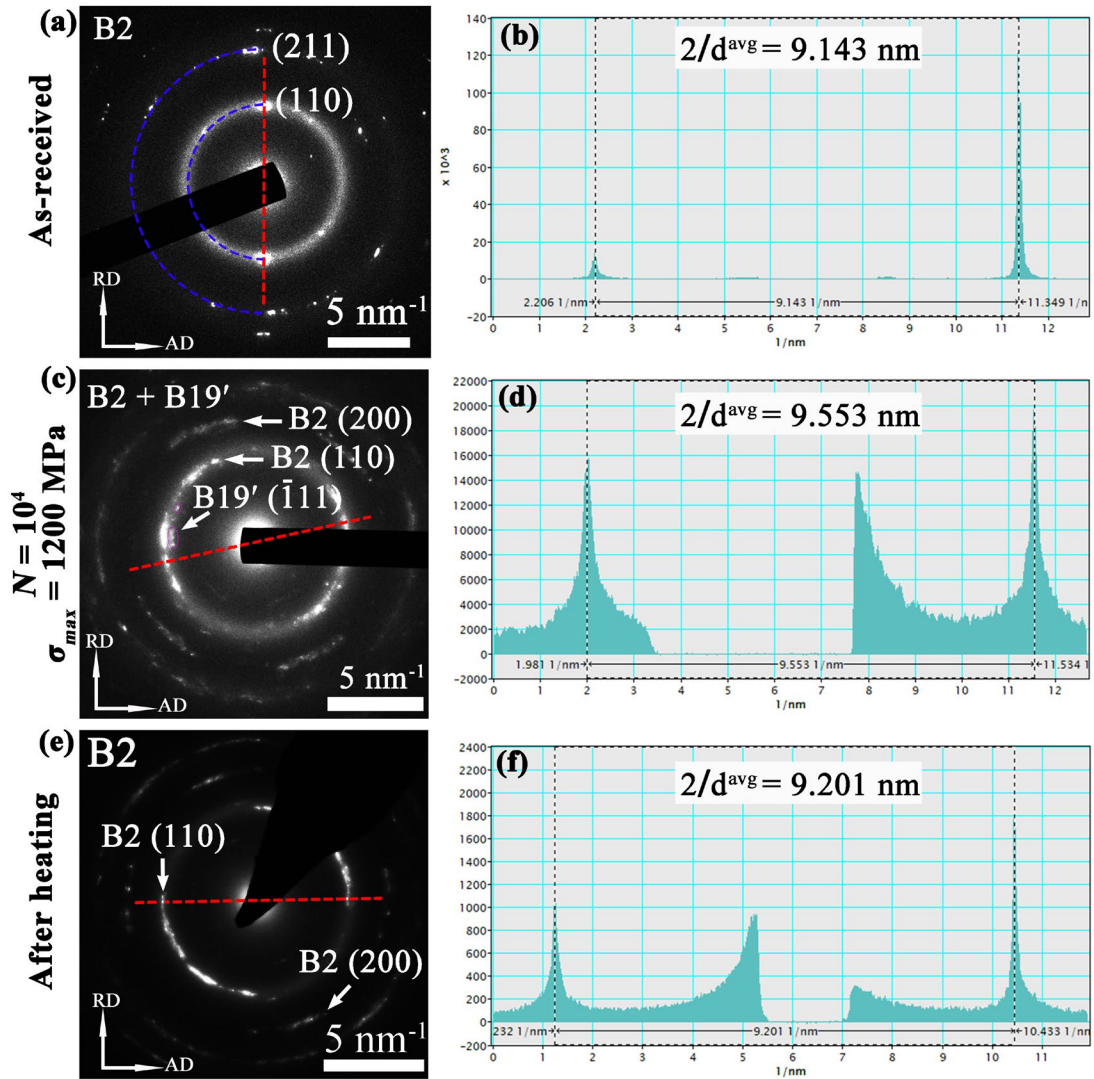


Fig. S8. SADP of as-received tube (a), deformed tube (c) and the deformed tube after heating (e); (b), (d) and (f) corresponding line profile of the red line in (a), (c) and (e).

10. Relation between hysteresis loop area and difference of $\Delta\sigma^{tr}$

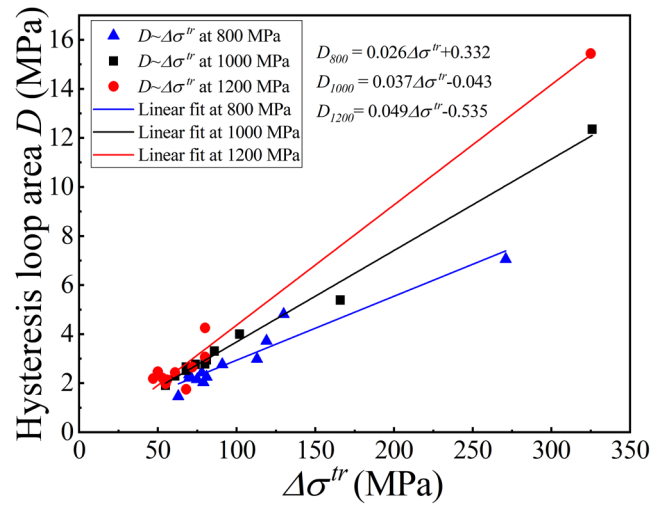


Fig. S9. Relationship of hysteresis loop area and difference of σ_f^{tr} and σ_r^{tr} .

11. The COP measurements at $N=1$ and $N=10^4$

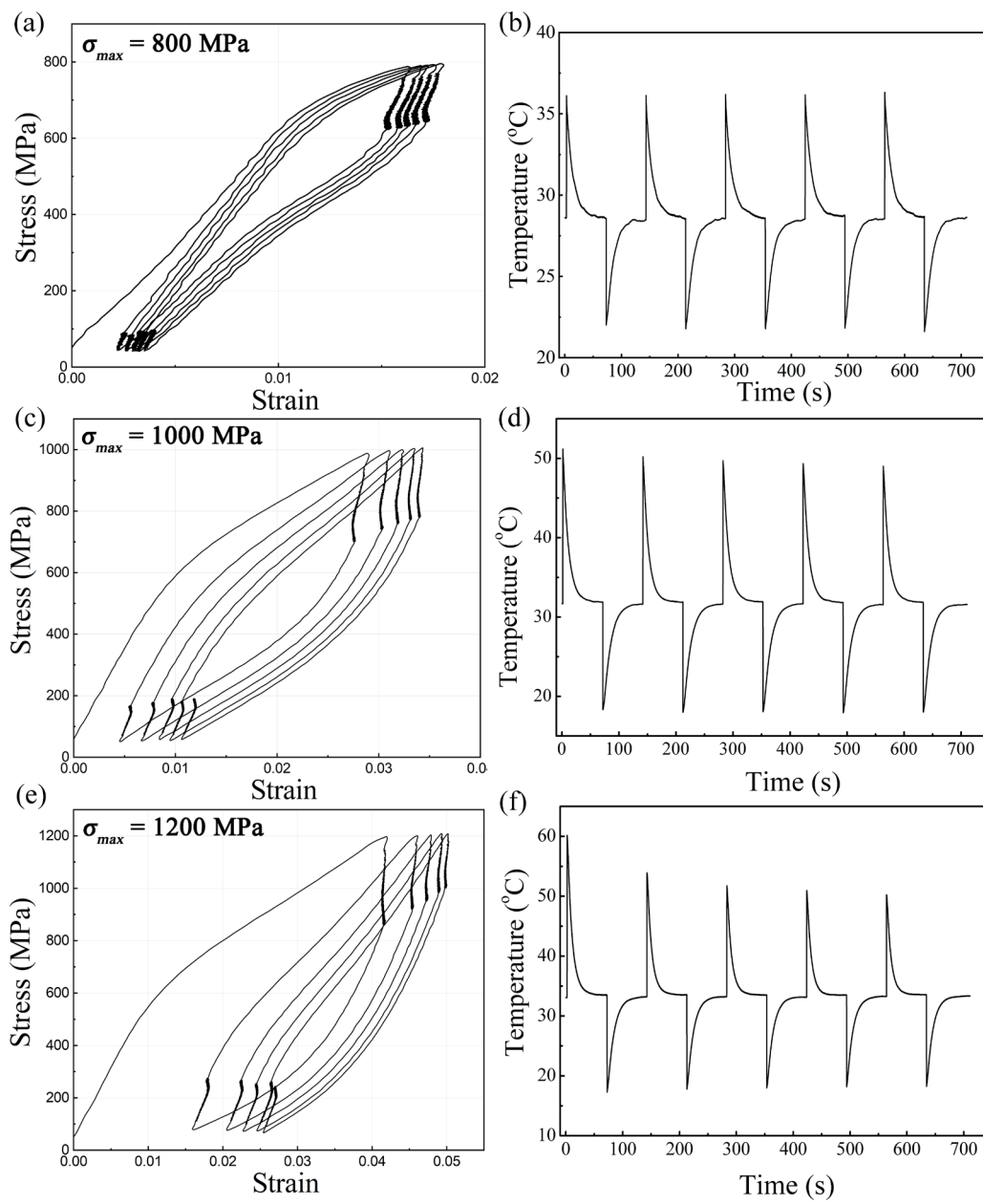


Fig. S10. Mechanical response at $N = 1$ for COP measurement under σ_{max} of 800 MPa (a), 1000MPa (c) and 1200 MPa (e); *In situ* temperature profile as a function of time under σ_{max} of 800 MPa (b), 1000MPa (d) and 1200 MPa (f).

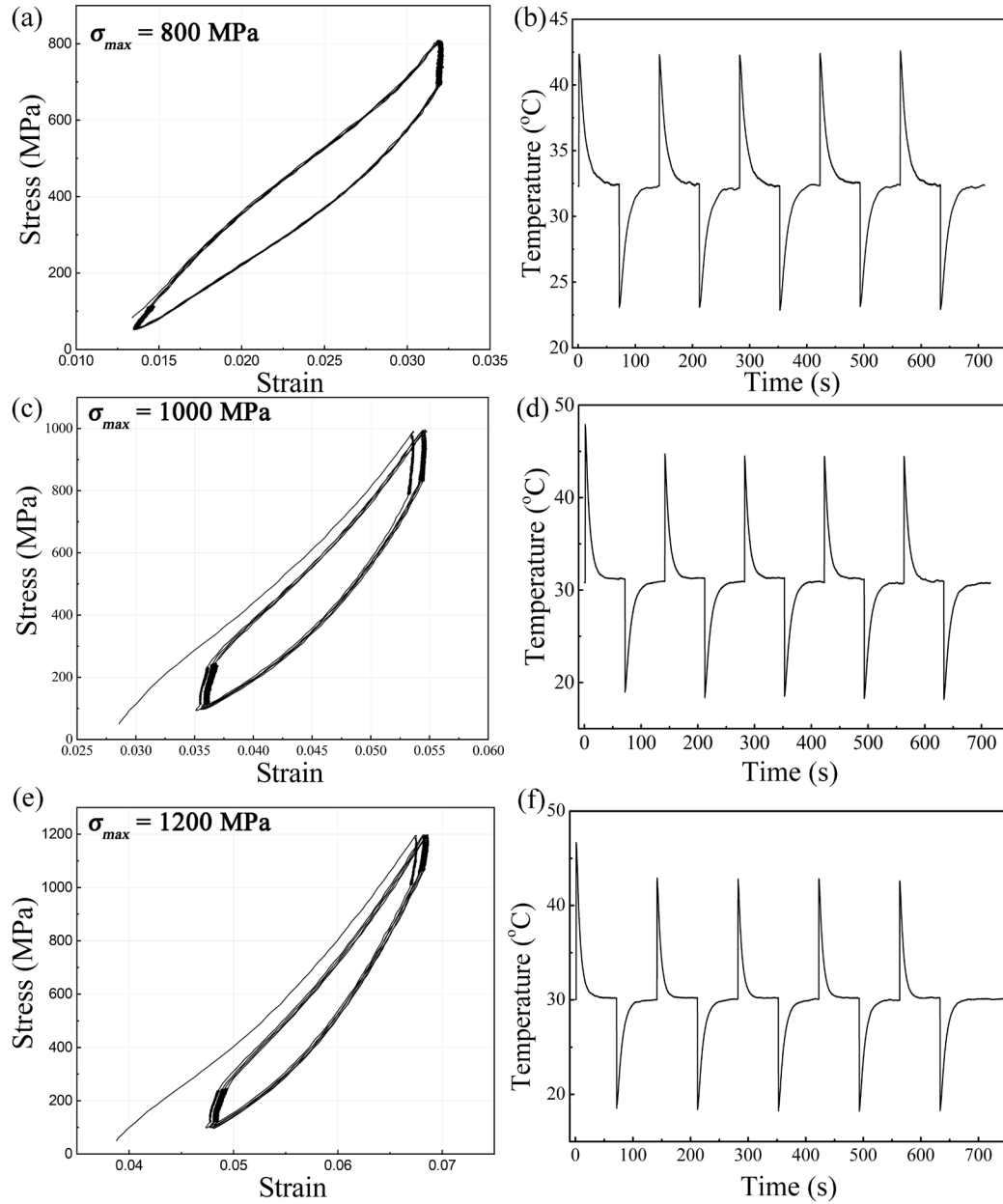


Fig. S11. Mechanical response at $N = 10^4$ for COP measurement under σ_{max} of 800 MPa (a), 1000MPa (c) and 1200 MPa (e); *In situ* temperature profile as a function of time under σ_{max} of 800 MPa (b), 1000 MPa (d) and 1200 MPa (f).

12. Lattice strain estimated by geometric phase analysis

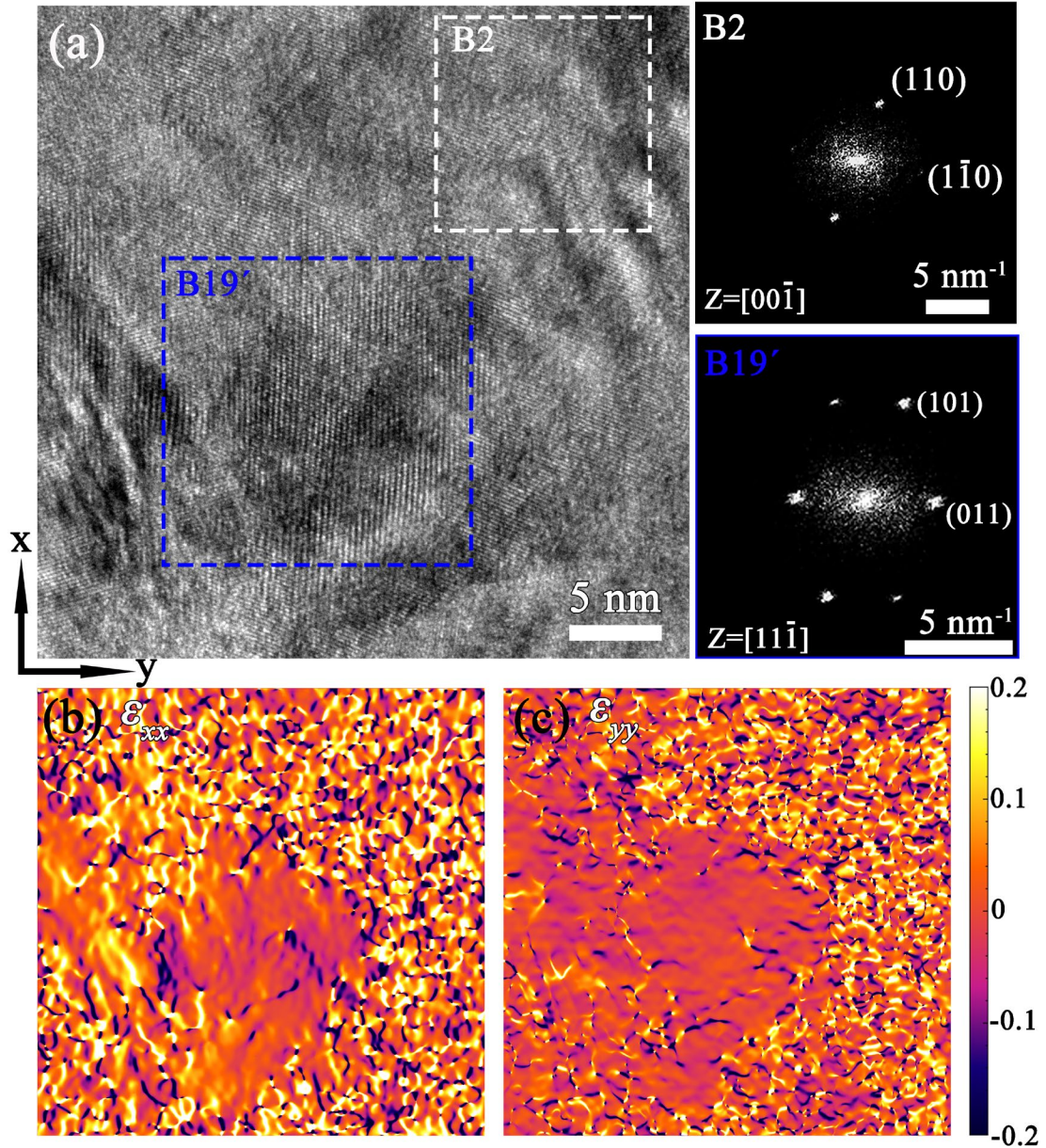


Fig. S12. Lattice strain estimated by geometric phase analysis via Strain++ [3] after 10^4 under 1200 MPa. (a) High resolution TEM of B2 and B19'; (b) estimated ϵ_{xx} ; (c) estimated ϵ_{yy} . The strain field in B2 is in a chaos of compressive and tensile strain , randomly distributing at the sub-nano scale. However, it is basically tensile strain in B19', despite highly localized compressive strain at the phase boundaries. Such qualitative estimation is consistent to the discussions of the main text.

Reference

- [1] S.P. Timoshenko, J.M. Gere, W. Prager, Theory of Elastic Stability, Second Edition, J. Appl. Mech. 29(1) (1962) 220-221.
- [2] P. Šittner, L. Heller, J. Pilch, C. Curfs, T. Alonso, D. Favier, Young's Modulus of Austenite and Martensite Phases in Superelastic NiTi Wires, J. Mater. Eng. Perform. 23(7) (2014) 2303-2314.
- [3] M.J. Hýtch, E. Snoeck, R. Kilaas, Quantitative measurement of displacement and strain fields from HREM micrographs, Ultramicroscopy 74(3) (1998) 131-146.